THESIS FOR THE DEGREE OF LICENTIATE OF ENGINEERING

The Process Atmosphere as a Parameter in the Laser-Powder Bed Fusion Process

CAMILLE PAUZON

Department of Industrial and Materials Science
CHALMERS UNIVERSITY OF TECHNOLOGY
Gothenburg, Sweden 2019

The Process Atmosphere as a Parameter in the Laser-Powder Bed Fusion Process
Camille Pauzon

No. IMS-2019-5

Department of Industrial and Materials Science
Chalmers University of Technology
SE-412 96 Gothenburg
Sweden
Telephone + 46 (0)31-772 1000

Cover: Microstructure of 316L stainless steel built by Laser-Powder Bed Fusion.

Printed by Chalmers Reproservice
Gothenburg, Sweden 2019

The Process Atmosphere as a Parameter in the Laser-Powder Bed Fusion Process

CAMILLE PAUZON

Department of Industrial and Materials Science

Chalmers University of Technology

Abstract

Laser-Powder Bed Fusion (L-PBF) is an Additive Manufacturing (AM) technique that allows to produce near-net shape components of complex design. Applied to metallic materials, L-PBF allows to consolidate subsequent layers of powder using the heat from laser radiation. The powder particles are typically micron-sized and have a high specific surface area, making them prone to surface oxidation.

As several layers are consolidated, the powder feedstock and solidified material are exposed to repeated thermal cycles, involving high peak temperatures and high heating/cooling rates. This heat input is likely to trigger oxidation by enhancing the reaction of the heated material with the residual oxygen present in the process atmosphere. To limit the extent of oxidation, protective atmospheres are used. These atmospheres are typically established by blanketing the powder bed using an inert gas, which permits the dilution of the present oxygen, and to some extent other impurities such as nitrogen and humidity. The gas will also drag away possible process by-products that are likely to introduce defects within the material upon their re-deposition. Although the gas is necessary for the L-PBF process, its role has mainly been disregarded until now as focus has been placed on other process parameters such as laser related ones (*e.g.* laser power and scanning speed). As a result, the available gases for L-PBF are limited to the noble argon and the relatively inert nitrogen, leading to the L-PBF machines being designed only for the use of these gases.

The present study aims to raise awareness of the significant role of the gas properties and control for the L-PBF process. The effect of the residual oxygen and processing gas properties are addressed. The results highlight that the residual oxygen guidelines should be proposed based on the sensitivity of the material to the oxygen and nitrogen exposure. While Ti-6Al-4V shows a difference in density at 1000 ppm O_2 compared to 100 ppm O_2, 316L stainless steel exhibits consistent mechanical properties for any oxygen level below 1000 ppm O_2. Upon higher oxygen partial pressure (*e.g.* 2000 ppm O_2), the 316L stainless steel powder particles develop oxide features on the surface. These features are consistent with an increased oxygen pick-up by the material, and the further reduction of its impact toughness, reflecting an increase in oxide inclusions content within the built material. Furthermore, the work conducted in this thesis gives an insight on the effect of the gas density and thermal properties on the produced Ti-6Al-4V material. Helium gas, which is significantly lighter than argon and nitrogen, was successfully implemented in the L-PBF process of Ti-6Al-4V. Helium and argon-helium gas mixtures enable a reduction in the porosity upon higher build rates. This is attributed to the positive balance of density and thermal properties offered by these mixtures. The obtained results could be used to initiate the development of new gas mixtures aiming at increasing the L-PBF productivity and process robustness.

Keywords: Additive Manufacturing, Laser-Powder Bed Fusion, processing atmosphere, process control, process stability, powder degradation, 316L stainless steel, Ti-6Al-4V

Preface

The work presented in this licentiate thesis was conducted at the Department of Industrial and Materials Science and the Linde Global Development Centre for Additive Manufacturing in Germany between October 2016 and December 2018. Most of the experimental activities have been performed during an 18 months research stay within Linde. The work was conducted in the framework of the Centre for Additive Manufacturing – Metal (CAM2), supported by Vinnova, and financially supported by Linde AG. The research has been carried out under the supervision of Professor Eduard Hryha, Professor Lars Nyborg at Chalmers and Pierre Forêt at Linde.

The thesis consists of an introductory part with an emphasis on the gas-related aspects for the Laser-Powder Bed Fusion process, followed by a summary of the work performed, given in the appended papers.

Paper I: **Effect of Argon and Nitrogen Atmospheres of Different Purities on the Properties of Stainless Steel 316L Parts Produced by Laser-Powder Bed Fusion**

C. Pauzon, E. Hryha, P. Forêt, L. Nyborg

Manuscript to be submitted

Paper II: **Effect of Helium - Argon Mixtures as Laser-Powder Bed Fusion Processing Atmospheres on the Properties of the Built Ti-6Al-4V Parts**

C. Pauzon, P. Forêt, E. Hryha, T. Arunprasad

Proceedings of WorldPM2018 World Congress on Powder Metallurgy

Beijing, China, Sept. 16-20, 2018, pp. 1633-1639, EPMA, 2018

Paper III: **Effect of the Laser-Powder Bed Fusion Gas Density and Thermal Properties on the Produced Ti-6Al-4V Parts**

C. Pauzon, P. Forêt, E. Hryha, T. Arunprasad, L. Nyborg

Manuscript to be submitted

Contribution to the appended papers:

Paper I: The author planned and conducted the experimental work and wrote the paper in collaboration with the co-authors.

Paper II: The author planned and conducted most of the experimental work and wrote the paper in collaboration with the co-authors.

Paper III: The author planned and conducted most of the experimental work. The author analysed the results and wrote the paper with the help of the co-authors.

Contents

Abbreviations

AM	Additive Manufacturing
ASTM	American Society for Testing Material
BSE	Backscattered Electrons
CAD	Computer-Aided Design
EDX	Energy-Dispersive X-ray spectroscopy
GA	Gas Atomization
HIP	Hot Isostatic Pressing
HR-SEM	High-Resolution Scanning Electron Microscopy
LOM	Light Optical Microscopy
L-PBF	Laser-Powder Bed Fusion
NTP	Normal Temperature and Pressure
OM	Powder Metallurgy
PSA	Pressure Swing Adsorption
PSD	Particle Size Distribution
SE	Secondary Electrons
STL	STereo-Lithography
TGA	Thermogravimetry Analysis
XRD	X-Ray Diffraction

Chapter 1: Introduction

Additive Manufacturing (AM) is defined by the ASTM F2792 standard as a ‘‘process of joining materials to make objects from 3D model data, usually layer upon layer, as opposed to subtractive manufacturing methodologies” [1]. It offers the opportunity to build parts with complex features in a limited amount of processing steps. Initially used within the aerospace, medical and automotive fields, it is appreciated by the greater audience because of its customization asset, and thus is now being adopted by industries such as fashion, jewellery, architecture, etc.

As with other AM processes, Laser-Powder Bed Fusion (L-PBF) has many process parameters associated to material properties that affect the quality of the built parts. So far, experimental observations were conducted to deepen the understanding of the effect of the combination of such parameters on the physical and mechanical properties of the produced material. This aims at enhancing and controlling the quality of the L-PBF products, by developing parametric guidelines [2]. The demand for these guidelines is increasing as efforts are put into process standardization and implementation across many industrial segments. Improved quality and control will allow to establish L-PBF as a robust process. A robust process means a process for which the defect generation is understood and can be limited. In order to make the process competitive with regards to other traditional processes, the challenge of productivity must also be addressed.

This challenge is supported by the development of process control and monitoring techniques. The control techniques allow to verify that the input parameters are properly implemented, such as using thermocouples to measure the temperature of the workpiece. The monitoring techniques aim at detecting possible process instabilities and to correct them. Process instabilities is a relatively extensive term that covers different events leading to defect generation impairing the properties of the produced material, for example, an uneven powder bed. The challenge resides in identifying the origin of these instabilities and finding the necessary corrective action. The development of these process control and monitoring tools comes hand in hand with the identification of influential process parameters.

Inert gases play a significant role along the process chain of the L-PBF process, from the feed material production to the final heat treatment, through the laser process itself. For example, they are involved during the powder gas atomization (GA) to protect the melted ingots from oxidation, and as highly pressurized gas streams to produce the metal droplets which solidify into relatively spherical particles upon cooling. Besides, there is the inert gas or the atmosphere under which the produced powder is subsequently packed, shipped, stored and handled and which may affect its degradation. Finally, inert gases are also involved in some of the post-processing steps such as heat treatment and hot isostatic pressing (HIP).

The gas as a process parameter has, to great extent, been overlooked in favour of the material and laser-related parameters such as the powder flowability, the laser power, the scanning speed, etc. As a result, limited understanding of the effect of the gas properties on the properties of the produced material has been gathered.

Still, within the L-PBF research community, there is no doubt that the protective atmosphere is necessary for several reasons: to limit the oxidation of the material, both the produced material and the used feedstock, to ensure a clean laser path by removing process by-products from the interaction area, and finally, to remove the heat generated at the melt pool. The short interaction time between the laser and the material yield a dynamic melt pool, solidifying rapidly. As a result, the above presented roles of the gas are co-dependent. Custom practice includes the use of argon and/or nitrogen. Most of the equipment manufacturers provide material specific guidelines, essentially limiting the use of nitrogen for materials sensitive to nitrogen pick-up, such as Ti-6Al-4V alloy.

1.1. Research objectives

The research objective of the presented work is to understand the effect of the process atmosphere characteristics on the stability of the L-PBF process by studying the defect generation and produced material properties. Specific addressed questions are defined as follows:

- What is the effect of the atmosphere purity on the properties of 316L stainless steel?
- What is the effect of the standard gases – argon or nitrogen – on the properties of 316L stainless steel?
- What is the effect of argon-helium gas mixtures on the process stability and properties of Ti-6Al-4V?

Chapter 2: Metal Additive Manufacturing

As opposed to traditional subtractive techniques, AM consists in adding material layer upon layer, instead of removing it, to produce parts of complex geometries. Described by the ASTM F2792 [1], AM processes can be divided into seven main groups of technologies:

- binder jetting
- directed energy deposition
- material extrusion
- material jetting
- powder bed fusion
- sheet lamination
- vat photopolymerization

AM covers a wide range of materials and opportunities to produce complex near-net shape parts of various sizes. In this work, the focus is on metal L-PBF.

2.1. Laser - Powder Bed Fusion

2.1.1. Forewords

Recently, AM and more particularly L-PBF, has drawn significant attention from the society, industrial and scientific communities. Among its advantages lies the production of customized goods, for instance tailored medical implants. The possibility to create complex features comes in hand with the new approach to design towards functionality. This is interesting for the aerospace and energy sectors, and the development of new lightweight components, sometimes replacing a prior assembly of parts. For example, Siemens produced an optimized gas turbine burner in one part instead of 13 individual pieces and 18 welds in its Swedish facilities (Finspång) [3]. Other benefits of the technology are the material utilization since minimum to no machining is required and the powder can be re-used to some extent. For this reason, the technology has been successfully adopted by the industry. As highlighted by Wohler's report 2017, the sales of metal AM systems increased significantly, from about 200 units in 2012 to 950 units in 2016 [4].

Within the AM community, Sweden places itself as a world leader of the metal powder production, with a well-established know-how in Powder Metallurgy (PM). Still, as the sales of metal AM systems increase, effort has to be brought to cope with the rising demand for metal powder volume and variety of available materials. In this context, understanding and development of the L-PBF process for specific material classes is of significant importance.

2.1.2. Principle

The L-PBF uses a laser as a heat source to selectively melt subsequent layers of powder and produce a part. Figure 1 displays the L-PBF process cycle, which can be divided into the pre-processing, the building of the part, and the post-processing. The powder recycling is often performed to enhance the material use.

The pre-processing consists of the data preparation of the part to be built. The design of the part can be created by a computer-aided design software (CAD). From the CAD file, an STL (STereo-Lithography) file is generated. The latter is a triangular representation into small surface elements of the design, which has to be placed within the virtual built volume (corresponding to the volume over the build plate), and further oriented, scaled, etc. This is generally done using a supplementary software. The manufacturers software allows to define the process parameters such as the layer thickness and then to slice the design accordingly. The information is gathered in a process file containing the necessary data, which is sent to the L-PBF machine. Before the process starts, the machine must be prepared by an operator, who will, for example, load the powder and conduct several adjustments.

The L-PBF machines usually consist of the following elements: an optical system (laser and scanning system), a powder dispenser platform, a building platform on which a build plate is mounted, a powder collector platform and a recoater to apply the powder, see Figure 1. These elements are placed into a volume called the process chamber. Right before the process is initiated, final adjustments of the level of the build plate relatively to the recoater are made. After the spreading of a thin layer of powder, the required process atmosphere (purity, composition) is established, typically by flushing the gas chamber with the process gas. The process is now able to start. The laser is turned on and will selectively scan some areas of the build plate, corresponding to the bulk of the input design. When this step is completed, the laser is turned off. The building platform is dropped by a layer thickness while the powder dispenser platform is raised. The recoater will rake the powder which is now above its level and spread it over the lowered build plate. The excess of the powder will be brought to the collector platform, which is also lowered during the process. The laser is turned on again to scan the following layer. This is repeated until the complete height of the part is reached.

Afterwards, the operator can open the process chamber and dismount the build plate, on which the parts are located, from the building platform. Some post-processing is necessary to remove the part from the plate and to achieve the possible parts requirements in terms of strength, surface quality, etc. Heat treatments can be applied for different purposes, *e.g.* stress relief, annealing, reaching a required microstructure, etc.

To start the next process, the machine has to be prepared again following a similar procedure. The powder accumulated in the collector and on the building platform has to be sieved prior to be re-used, to ensure a consistent particle size distribution (PSD).

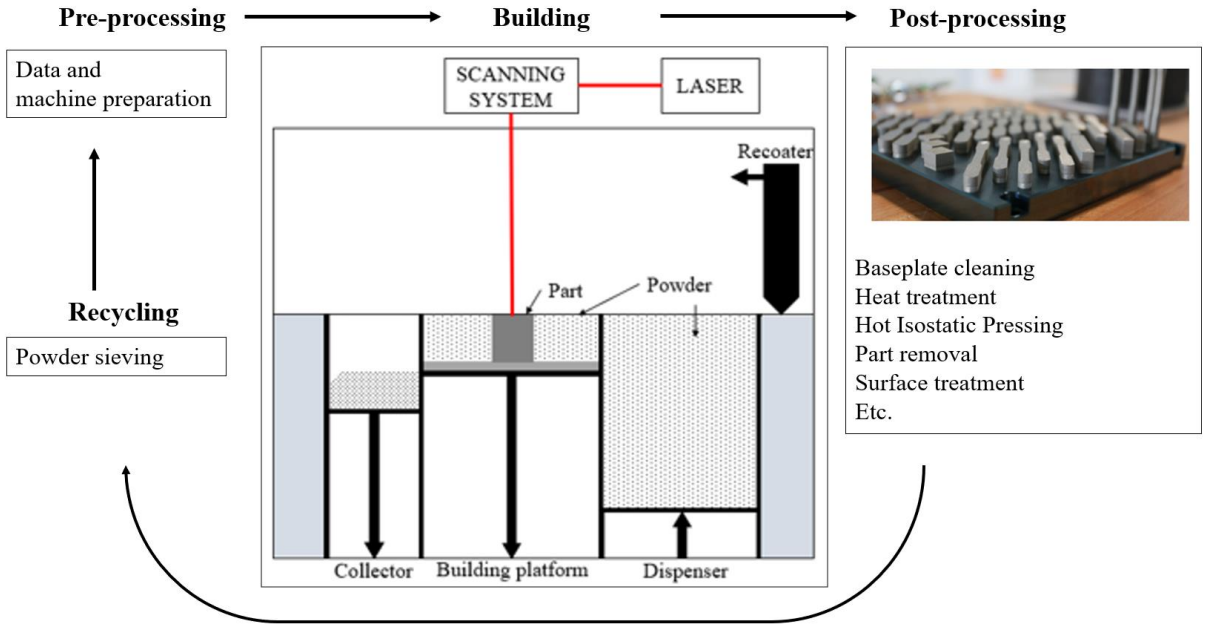

Figure 1: Process cycle of L-PBF.

Process atmosphere generation

When the L-PBF machine is prepared for a building sequence, the operator closes the chamber door. As a result, the initial atmosphere in the process chamber is the same as the ambient workshop atmosphere (*i.e.* similar humidity and composition). The gas will enter the chamber from an inlet which is a distributor that splits the main gas flow, ideally into a homogeneous flow covering the build plate towards an outlet. The design of the gas inlet is an active development activity for machine manufacturers to assure a homogeneous laminar gas flow over the whole build plate.

The generation of the process atmosphere is performed by purging the process chamber with some inert gas, typically argon or nitrogen. Two purging techniques can be identified among the different manufacturer's solutions: vacuum purge and simple purge. The vacuum purge consists in creating a vacuum within the chamber to remove most of the air and to back-fill it with inert gas. The vacuum purge may be repeated to achieve a given level of purity. The simple purge technique consists in purging the initial air of the chamber with inert gas, without prior vacuuming. The desired residual oxygen level is achieved by dilution of the impurities. This is the most commonly adopted technique.

The accuracy of the measured residual oxygen level may be influenced by the type of employed oxygen sensor, its calibration and its positioning with respect to the powder bed. Once the oxygen level requirement is fulfilled (defined by machine manufacturers), the machine generally recirculates the gas which passes through filter units. The filters are responsible to remove remaining particles from the gas flow. Finally, the speed of the gas is established using a feedback control system. Different machines may use different sensors to measure the gas speed. For example, it could be an anemometer, a hot wire, a pressure control system, etc.

2.1.3. Building parameters

As highlighted in Figure 1, the produced part properties are dependent on the pre-processing, the building, the post-processing and the powder recycling procedures. This may explain how parts produced with the same machine and process parameters result in different properties. Most machine manufacturers provide their customers with material specific parameters. A set of parameters covers laser settings such as the laser power, the scanning speed and the hatch distance (distance between two laser passes), but also the powder layer thickness. These are the main parameters the operator usually tunes during process optimization.

The build rate can be defined as the product of the scanning speed, the hatch distance and the layer thickness. It gives an idea of the volume of material exposed to the laser radiation, although not necessarily solidified and densified. The achieved density for a given build rate will depend on the combination of the process parameters as well as the properties of the powder feedstock. Productivity can be understood as increasing the build rate without compromising the quality of the produced part in terms of density, defect distribution and mechanical properties.

Many more process variables exist and can be considered, among which, the building platform temperature, the speed of the recoater, the amount of dispensed powder, the order followed to scan different parts, etc. The so-called building strategy is also defined within the parameter set. It corresponds to the definition of the laser path within the area to be scanned. The individual and combined influence of these parameters are not yet tackled. And the gas as a process variable is mostly underestimated, although some authors have recently highlighted its relevance [5], [6]. In the following sections, the gas properties as well as the interaction of the gas with the laser and the metal powder during the process, will be addressed.

2.2. Properties of the gas

Argon and nitrogen gas are usually employed to establish the process atmosphere of L-PBF machines. Argon with its full outer shell of electrons is a noble gas, while nitrogen is present in the air as a diatomic molecule. Like argon, the nitrogen molecule has no free electrons and is relatively inert. Still, it can dissociate and be dissolved in the metal in its atomic state. The nitrogen atoms can then react with other elements such as oxygen, hydrogen or sulphur and alloying elements.

Together with oxygen (20.95 %), nitrogen (78.08 %) and argon (0.93 %) are the main constituents of the Earth´s atmosphere. Argon mainly originates from the radioactive decay of potassium 40. On the other hand, nitrogen present in the primitive atmosphere of the Earth (*e.g.* produced from volcanoes)

did not react significantly since then, and that explains its major contribution to today´s atmosphere. Both argon and nitrogen can be extracted from air by different means resulting in different qualities, *i.e.* amount of residual impurities in the extracted gas. The fractional distillation of liquid air allows to extract both, argon and nitrogen. In this process, the air is cooled until it liquefies and the different components are separated thanks to their different boiling temperatures. By doing so, high quality gases are produced, *i.e.* less than 10 ppm impurities.

Many gas supply solutions are available to run L-PBF machines. Nitrogen, that is more abundant, can also be produced from gaseous air using the pressure swing adsorption (PSA) technology. In this technique adsorptive materials act as traps to selectively adsorb specific gas species. Polymeric membranes, that are permeable fibres filtering the air, can also be used to produce nitrogen gas from ambient air. Utilisation of these mechanical solutions to produce nitrogen generally results in intermediate gas qualities, in the range of 10 ppm to 10 000 ppm impurities for the PSA technology and 1 000 ppm to 50 000 ppm impurities for membranes, depending on the incoming amount and pressure of air.

Helium, belonging to group 18 in the periodic table, is a noble gas like argon. Even though it is the second most abundant element in the Universe after hydrogen, mostly produced during the Big Bang nucleosynthesis, its presence on Earth remains limited, *i.e.* about 1 ppm in the air [7]. On Earth, most of it arises from the radioactive decay of heavy elements such as uranium or thorium in Earth´s crust. The radiated particles may find a way to the atmosphere or, more likely, get trapped between impermeable layers of rock where natural gas accumulates. Therefore, helium is mainly obtained by fractional distillation of natural gas, which may contain up to 4 % of helium in volume fraction [7]. Table 1 displays some of the interesting properties of the gases considered in this thesis study.

Table 1: Processing gas properties considered in this study at NTP (Normal Temperature and Pressure, i.e. 20 ºC and 1 atm)

Gas	**Density [kg/m^3]**	**Specific heat capacity at constant pressure [J/(kg·K)]**	**Volumetric heat capacity [J/(m^3·K)]**	**Thermal conductivity [W/(m·K)] at 25 ºC**
Argon	1.62	520	842	0.016
Nitrogen	1.14	1040	1186	0.024
Helium	0.16	5190	830	0.142
Argon:Helium (50/50)	0.91	940[1]	855	0.040 to 0.070[2]
Argon:Helium (70/30)	1.21	707[1]	855	0.020 to 0.040[2]

The specific heat capacity is the heat required to raise the temperature of 1 kg of the considered gas by 1 Kelvin. The thermal conductivity is a measurement of the ability to conduct heat. In other words, it describes the rate at which the energy will be transferred within the gas. These properties are temperature dependent and will vary with the laser heat input. The specific heat capacity and thermal conductivity increase with the temperature, while density will decrease. For gas mixtures, the specific heat capacity can be calculated with the rule of mixtures. However, the thermal conductivity of gas mixtures is a research area of its own. Models based on the kinetic theory of gases have been developed, such as the Chapman-Enskog method. The experimental work performed by Clifford *et al.* [8] allows to evaluate the thermal conductivity of the argon-helium mixtures.

From Table 1 it can be inferred that helium will have a lower temperature than argon for the same heat input coming from the laser or the heated material due to its high specific heat capacity. Besides, this

[1] The specific heat capacity of the mixture is calculated using respective mass fractions and specific heat capacities.
[2] Thermal conductivity is not as straight forward to derive as the specific heat capacity. The displayed range is defined according to the experimental work performed by Clifford *et al.* [8].

heat will be more readily dissipated within helium than within argon thanks to its higher thermal conductivity. Nitrogen offers a higher specific heat capacity than argon for a similar density and thermal conductivity. The mixtures of argon and helium provide an interesting trade-off between density and thermal conductivity.

Considering the properties presented in Table 1, the heat capacity rate (C) of the gases can be derived. It is defined as the product of the specific heat capacity and the mass flow rate, see Equation (1):

$$C = C_p \quad \frac{dm}{dt} = C_p \, \rho_{gas} \, v_{gas} \, A \tag{1}$$

Where C_p is the specific heat capacity, $\frac{dm}{dt}$ is the mass flow rate, ρ_{gas} is the gas density, v_{gas} is the gas speed, and A is the crossed area, which is machine dependent and does not vary for the different gases. The heat capacity rate corresponds to the quantity of heat the flowing gas can absorb per unit time and per unit of temperature change. The mass flow rate is the product of the gas density, the gas speed and the considered surface crossed by the gas. The product of the specific heat capacity by the gas density gives the volumetric heat capacity listed in Table 1. The latter does not vary significantly among the gases. Considering that the gas speed is kept constant, it can be expected that the ability of the different gases to dissipate heat is relatively similar. However, the thermal conductivity and density are significantly different and may still influence the heat transfer. This will be addressed after giving deeper insight on the laser – powder interaction, see Section 2.3.3.

2.3. Laser – powder – gas interaction

2.3.1. Melt pool formation

During the laser exposure time, the incoming radiation passes through the gas media, and is absorbed by the metal target (powder particles or already solidified material). The presence of a layer of powder on top of the build plate promotes the laser absorption by multiple reflections and scattering on the surface of the particles [9]. This leads to a better optical penetration depth compared to the use of bulk material [10].

As explained by Simchi [10], within the L-PBF scanning speed range (*i.e.* 50 to 7000 mm/s), the exposure period to the laser radiation varies from 0.2 to 8 ms. As a result, the interaction time is short, and the heat flow distance is much smaller than the particle diameter. In turn, the particles surface heats up very quickly. This is followed by a homogenization phase, during which the heat diffuses from the skin of the particle to its core. Later, the heat diffuses into the powder bed of lower thermal conductivity. It is the cooling phase described by Fischer *et al.* [11].

When the metal temperature is higher than its melting temperature, it undergoes a transition from solid to liquid state and the melt pool is formed. The transfer of the heat from the melt pool to its surrounding occurs by radiation, conduction and convection. The radiation is the main input data of available monitoring systems. The conduction mainly occurs through the already solidified material, the powder bed and the atmosphere. The convection results from different driving forces. Dikshit and Bhatia [12] identified the following main contributions to convection: the surface tension, the buoyancy and the vaporization.

The temperature profile of the melt pool describes a gradient with the highest temperature at the laser beam spot. As the surface tension decreases with increasing temperature, the centre of the melt pool is characterized by a lower surface tension than the edges. The surface tension gradient induces a liquid flow from low surface tension areas to the high surface tension areas (*i.e.* outward movement). This is the so-called Marangoni flow. For the low laser scan speeds, more energy input is delivered to the

material, which in turns can intensify the Marangoni flow and cause turbulences within the melt pool [13]. As the metal density will decrease with the increasing temperature, buoyancy will also drive the fluid outward, similarly as the Marangoni flow. Besides, the effect of surface-active elements such as oxygen or sulphur and nitrogen should not be undermined [14], [15]. Present in ppm levels at the melt pool surface, they may reverse the Marangoni flow (*i.e.* inward movement).

As the metal surface temperature increases, the sublimation and vaporization of the metal increases exponentially, see Figure 2. They are dependent on the atmosphere pressure [16]. Figure 2 displays the vapour pressure curves of some elements present in the metal systems studied. In addition, low pressure on top of the melt pool will decrease the boiling point of the alloy as well. Upon higher pressure, less heat is lost into sublimation and vaporization and the melt pool temperature can be expected to be higher. However, for some elements the vapour pressure can exceed the pressure of the processing gas on top of the melt pool in case of significant melt pool overheating, see Figure 2.

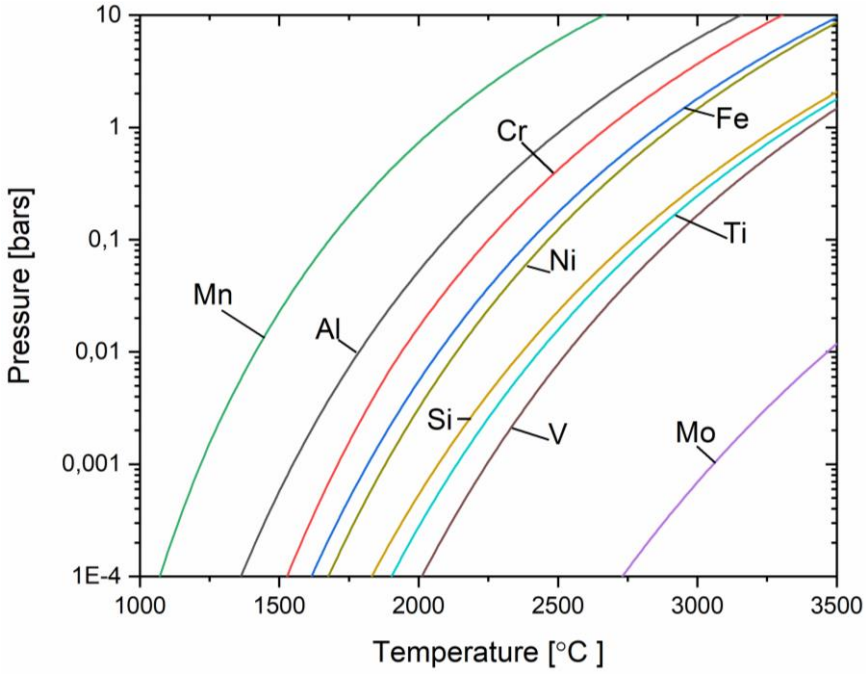

Figure 2: Vapour pressure curves for elements present in the studied systems (plotted with HSC Chemistry).

Hence, in most of the laser processes connected with metal heating up to fusion, metal vapours are formed above the surface [17]. The metal vapour expands vertically against the ambient gas [18]. The metal vapours have a high temperature and hence the free surface of the molten pool is covered by a high temperature gas, that in turns applies a pressure on the surface as it expands. It is the so-called recoil pressure, and it is responsible for the outward movement of the liquid within the melt pool. For high enough recoil pressure, a cavity forms, the keyhole. Light absorption is enhanced by multiple scattering on the keyhole walls [19]. The laser absorption is enhanced up to a certain point, when the laser radiation may be absorbed or reflected by the formed vapours before hitting the keyhole. This is a saturation level.

If the gas enhances the heat dissipation by conduction, it is likely that the temperature at the melt pool will drop faster and the Marangoni flow and vaporization will be reduced. Still, the gas pressure is an important factor for the vaporization. Figure 3 displays the above mention phenomenon responsible for heat convection within the melt pool.

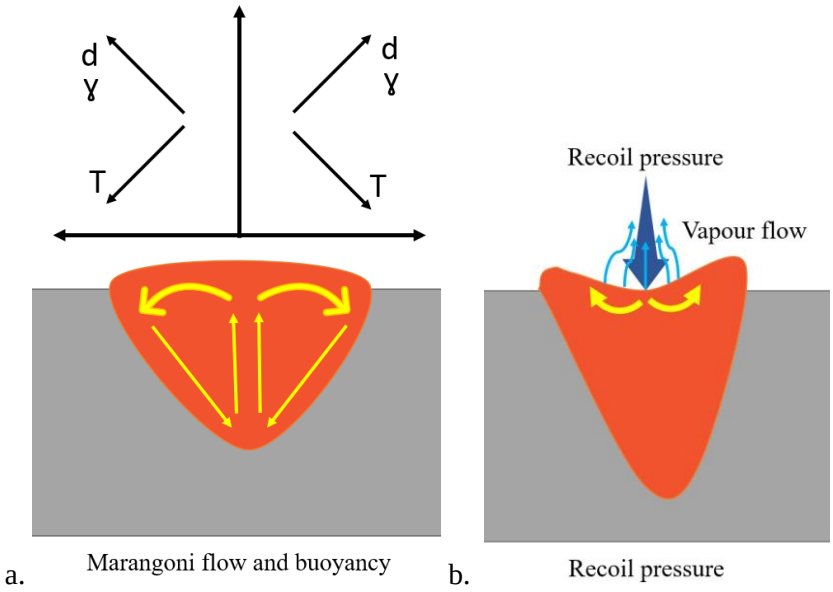

Figure 3: Schematic representation of the convection within the melt pool: a. due to the temperature dependent surface tension and density; b. due to the vaporization.

It has recently been shown that the vapour flow results in a local pressure drop above the melt pool that creates a lateral gas flow, following Bernoulli's principle [20]. The latter can pull surrounding metal particles from the powder bed into the melt pool, generating a so-called denudation zone around the scanned area, where the number of metal particles is reduced.

2.3.2. Process by-products generation

As the process runs, one may observe some projections, see Figure 4. These only account for the light emitted in the visible range. Their detailed observation requires high magnification and high-speed cameras, possibly thermal cameras. Indeed, Bidare *et al.* [21] reported that the speed of projections is in the range of tens of m/s. Such in-situ observations are limited by the exposure time and the lightning of the zone of interest. By-products may arise from different sources and come in different sizes and shapes. In this section, the possible emission causes and the resulting interactions of the projections with the laser beam are considered.

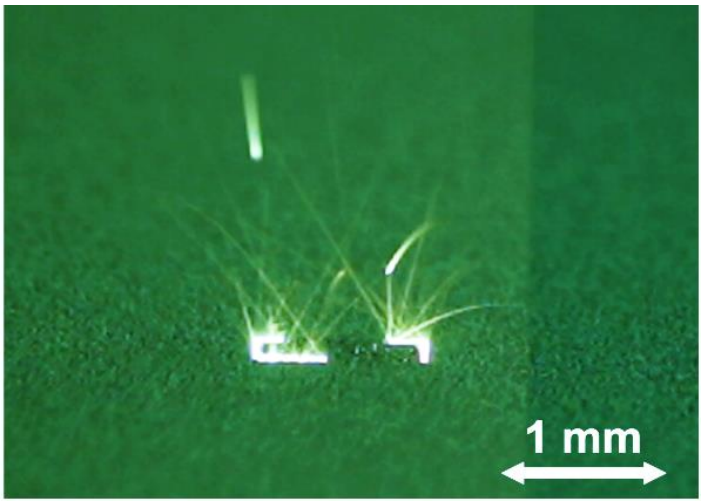

Figure 4: Process snapshot taken during the laser scanning with a Canon D1000 camera and 316L stainless steel powder in EOS M290 machine.

The local heating of the powder bed by the laser may result in the rapid expansion of the gas in the inter-particle spacing and can expel neighbouring particles. These accelerated particles can be ejected at

different angles and be taken in the gas stream, fall in the powder bed, or intersect the laser beam. Projections may also arise if forces within the melt pool overcome its surface tension. These forces may come from an important Marangoni flow or because of the recoil pressure [19]. Finally, vapours produced by the vaporization of low boiling point alloying elements, are likely to condense by reacting with the available oxygen within the atmosphere and form fumes, also called condensates.

The above-mentioned by-products interact with the process as follows. Expelled upwards, they can travel through the metal vapour flow or the laser beam. Ly *et al.* [22] called the first ones "cold particles" and the second ones "hot particles". The particles passing through the laser beam may cause laser shadowing by absorption of the radiation, or also scattering, and thus defocusing of the laser. This reduces the energy input to the powder bed.

In general, the by-products have experienced relatively high temperatures, promoting the mass transfer of elements with high affinity to oxygen from the volume to the surface of the particle [23]. The re-deposition of these highly oxidized particles within the powder bed may have major consequences. If such particles fall on areas to be laser scanned, it could be that the laser energy is not enough to fully melt the oxides. This can lead to oxide inclusions and in severe cases even to lack-of-fusion defects. If fully melted, the oxide may still introduce some oxygen enrichment detrimental to the homogeneity and composition of the material. If the oxidized particle falls on an area not scanned by the laser, it can still be a concern as the powder batch will be recycled. If the size of the given particle lies within the particle size distribution requirement, it will be retained in the feedstock, which may on the long-term lead to oxygen pick-up and increase of the appearance of inclusions and lack-of-fusion defects.

Figure 5 schematically summarizes the above mentioned phenomena. For all types of projections and fumes, it is desirable to have small size projections with high speeds. This will allow to limit the interaction of the laser and the re-depositions, and promote their removal by the process gas flow.

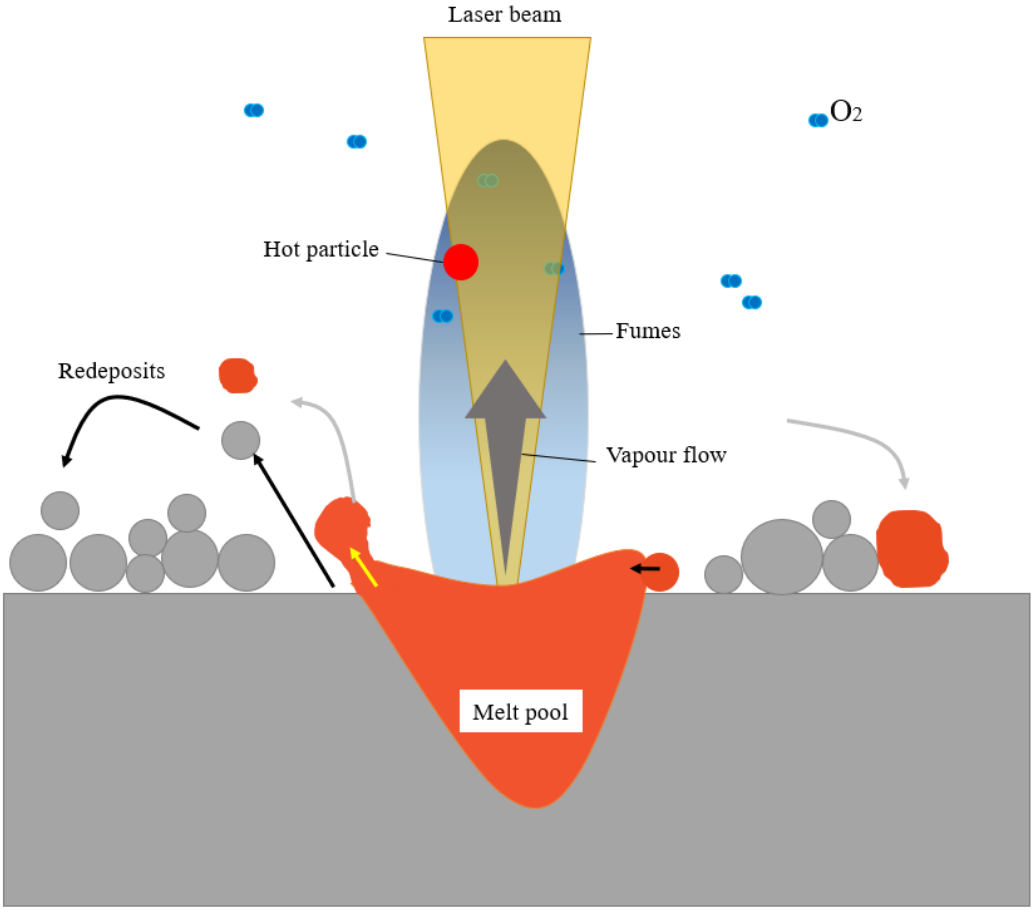

Figure 5: Scheme of the process by-products origins, based on [24].

2.3.3. Process by-products removal

The process gas must ensure that the previously described projections are properly disposed away from the interaction region by applying a force to take them towards the gas outlet. The interaction of the projection with the gas can be resumed as follow. As the particle is emitted at a given angle and with a given initial speed, it will be exposed to gravity ($\vec{F}_{gravity}$) and the drag force exerted by the gas ($\vec{F}_{gas}$).

Considering Newton´s second law, the motion of the projections is described by the following equation:

$$\ddot{\vec{x}} = \frac{1}{m} \sum \vec{F} = \frac{1}{m} \left(\vec{F}_{gravity} + \vec{F}_{gas}\right) = \left(\vec{g} + \frac{\vec{F}_{gas}}{m}\right) \quad (2)$$

Where $\ddot{\vec{x}}$ is the acceleration vector of the particle, m is the mass of the particle, and $\vec{g}$ is the gravity vector.

The drag force is given by:

$$\vec{F}_{gas} = \frac{1}{2} C_D \cdot \rho_{gas} \cdot A_{particle} \cdot \dot{\vec{x}}^2 \quad (3)$$

Where C_D is the drag coefficient (dimensionless and depending on the shape of the projection and the Reynolds number – which describes the flow), ρ_{gas} is the density of the gas, $A_{particle}$ is called the cross sectional reference area, and $\dot{\vec{x}}$ is the velocity vector.

The solution of the differential equation describing the motion of the projections will depend on the boundary conditions of the system. Among these boundary conditions, the morphology, density and size of the particle, as well as its emission angle and speed will be determinant. As the projections are small and light, the drag force is likely to play a major role on their removal. As highlighted by Equation (3), the gas drag force is proportional to its density. Still, a high drag force (high gas speed or gas density) may introduce friction forces on the powder bed and thus inhomogeneous powder layers. From Table 1, it may be inferred that the argon will apply the greatest drag force. The drag force of nitrogen and the mixture of argon and helium will be reduced, while that of helium will be significantly lowered.

The boundary conditions regarding the gas flow such as the velocity profile and its laminarity shall be considered. Schniedenharn and Schleifenbaum [25] showed that the L-PBF process by-products emitted from the melt pool have a high kinetic energy, so that they are not directly deviated from their initial emission direction. Later, their trajectory is falling back within the gas streamlines. Therefore, it is beneficial to have the maximum gas speed not directly at the melt pool level but slightly above. Two kinds of profiles along the building direction have been identified: the “b”-shaped profile with an inhomogeneous speed distribution and the maximum close to the baseplate; and the “D”-shaped profile with a more homogeneous distribution. According to the work conducted by Schniedenharn and Schleifenbaum [25], the “b”-shaped profile results in higher produced material densities than the “D”-shaped profile. Besides, Ferrar *et al.* [26] highlighted the importance of the gas flow uniformity over the build plate, to achieve low porosity independently from the position of the part on the building platform.

2.3.4. Effect of residual oxygen and nitrogen

The gas flow ensures a reduced oxygen level at the powder bed. While the process is running, the powder bed temperature increases significantly, especially at and close to the laser spot. This may result in the oxidation of the material exposed: the melted and solidified material, the powder particles surrounding melt pool and the projections. Both oxidation of solid and liquid metal can take place. Like oxygen, nitrogen molecules are present in a non-negligible amount and will interact at the metal/gas surface.

For a tight L-PBF system which recirculates the process gas, the oxygen and nitrogen content of the melted powder and of the initial atmosphere should be equal to that of the produced part, projections and produced gas due to *e.g.* oxide and nitride dissociation. The powder close to the part may also pick-up some oxygen and nitrogen. If the L-PBF system experiences leaks, more oxygen and nitrogen can make their way into the process chamber and react with the material. In the real systems, this issue is tackled using an additional gas holding flow, enabling to further dilute these impurities. In this section, aspects related to the oxygen and nitrogen pick-up are developed.

a. A few L-PBF-related considerations

The L-PBF process implies local and repeated high heating and cooling rates. The measure of the melt pool temperature is challenging. Direct measurement using for example thermocouples can be limited by the thermocouple temperature limit, the acquisition frequency of the logger, the reaction time of the thermocouple itself and the thermocouple positioning relatively to the location of interest. Some thermocouple measurements reported up to a few hundred degrees in peak temperature [27].

Indirect measurements, *e.g.* contactless, have mainly been conducted using thermal cameras. For example, Brandon *et al.* [28] could resolved up to 1025 ºC with their system, still lying below the real maximum temperature achieved at the melt pool. Finally, the simulation of the melt pool dynamics performed by King *et al.* [29] reports peak temperatures of about 4727 ºC and 2727 ºC when considering the evaporative losses. These studies support the high L-PBF cooling and heating rates – 10^5 - 10^7 K/s reported elsewhere in the literature [30]–[34]. This suggests that the temperature of the built material can remain relatively elevated during the process. It is estimated that each laser scan remelts 3 to 5 layers underneath. This can trigger diffusion mechanisms and bring the system closer to its equilibrium.

Similarly, the powder particles close to the hot material also experience the thermal cycles with reduced peak temperatures and high heating and cooling rates. The powder particles used for L-PBF have a large specific surface area and are very reactive. They are commonly covered with a thin oxide layer. The high temperatures experienced by the particles can enhance the growth of this oxide scale by mass transport of alloying elements with high oxygen activity to the powder surface, triggered by oxygen concentration gradient.

b. Oxygen and nitrogen dissolution

The dissolution of oxygen and nitrogen into the metal occurs by adsorption. When the molecules are adsorbed on the surface of the metal, they can dissociate and be adsorbed as atoms, which may dissolve in the metal matrix. The oxygen and nitrogen solubility limit will depend on their respective partial pressure and activity coefficient. The solubility will increase with the partial pressure and decrease with the activity coefficient increasing. The activity coefficient relies on the addition and effect of alloying elements. This information is today available within software packages such as ThermoCalc, based on the experimental databases.

Giuranno *et al.* [35] highlighted that the oxygen adsorption at the melt pool interface can be hindered by the evaporation of metal atoms and oxides already present at the interface. Similar effect can be expected for nitrogen molecules adsorption. Besides, the atoms that dissolve at the interface may stay in solution or form oxides floating at the melt pool surface or within the material. As highlighted by Giuranno *et al.* [35], the diffusion of oxygen within the melt will be influenced by convection, for example because of the Marangoni flow. In addition, oxygen and nitrogen solubility usually decrease at the solidification point, which may lead to the formation of gas porosity.

c. Secondary phases: oxides and nitrides

Stability of oxides

The change in free energy associated with the oxide formation is a measure of the metal oxidation potential, highlighting the oxide stability under given processing conditions. The oxide dissociation can be presented as follows:

$$\frac{2}{y}M_xO_y = \frac{2x}{y}M + O_2 \tag{4}$$

With M referring to the metal and M_xO_y to the oxide.

The corresponding change of standard Gibbs free energy of the system upon the reaction is given by:

$$\Delta G_1^0 = \frac{2x}{y}G^0(M) + G^0(O_2) - \frac{2}{y}G^0(M_xO_y) \tag{5}$$

A chemical reaction occurs when the change of standard Gibbs free energy is negative. It is therefore related to the equilibrium constant K, as follows:

$$\Delta G^0 = \Delta H^0 - T\Delta S^0 = -RTln(K) \tag{6}$$

Where ΔH^0 is the standard enthalpy change, T is the thermodynamic temperature, ΔS^0 is the standard entropy change, and R is the gas constant.

The equilibrium constant for the oxide dissociation is given by:

$$K = \frac{a^{\frac{2x}{y}} \cdot a(O_2)}{a^{\frac{y}{2}}(M_xO_y)} \tag{7}$$

With a the activities of the considered species involved in the reaction. The activity is the ratio of the vapour pressure of the specie in the given conditions and the vapour pressure of the pure solid or liquid substance under the same conditions. Hence the activity of a pure solid or liquid substance is unity, and the activity of ideal gases is equal to their partial pressures. For the reduction reaction on the surface of the powder, the activity of the pure metal and that of the oxide are unity, from where expression for the partial pressure of oxygen can be derived:

$$K = a(O_2) = p(O_2) = \exp\left(-\frac{\Delta G_1^0}{RT}\right) \tag{8}$$

The ΔG_1^0 values for different metal oxides can be calculated from the specific heat data or using thermodynamic simulation softwares. From these, the temperature dependence of the equilibrium partial pressure of oxygen can be represented as shown in Figure 6. Below each curve representing a metal/oxide system, the given oxide is decomposed, and above each curve it is thermodynamically stable. It can obviously be inferred that the oxygen partial pressure must be reduced by several orders of magnitude to promote dissociation for most of the oxides, or very high temperatures are required.

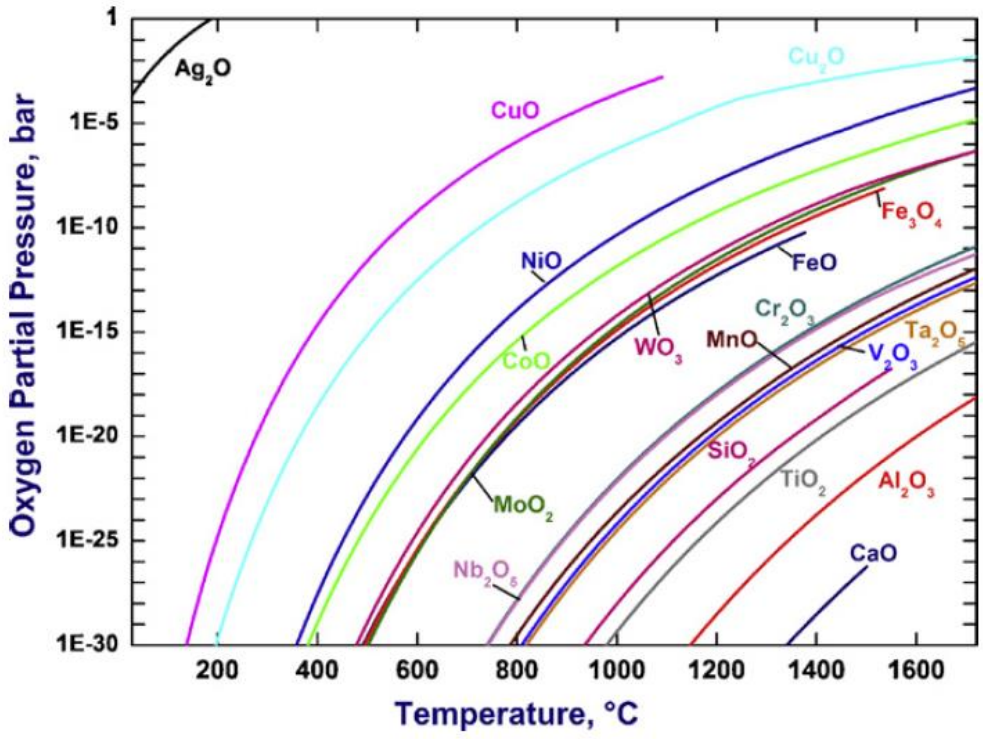

Figure 6: Equilibrium partial pressure of oxygen for some oxide/metal systems (plotted with HSC Chemistry) [36].

As previously mentioned, the standard L-PBF process runs under inert gas with a residual oxygen level of about 1000 ppm, *i.e.* 0.1 bar. This is a relatively high oxygen partial pressure for which a lot of oxides are stable, up to a high temperature, see Figure 6. Still, Figure 6 concerns pure metal-oxide systems under thermodynamical equilibrium and does not provide information about the oxidation kinetics that will influence the type and amount of oxide encountered.

It is difficult to study the oxidation rates occurring during L-PBF by traditional means such as thermogravimetry analysis (TGA). TGA allows to monitor the mass change of the heated metal which is due to the oxidation, under a specific temperature profile and atmosphere. However, the heating and cooling rates which apply globally to the sample are typically limited to up to 50 ºC/min, even though atmosphere composition can be controlled to simulate the gas composition in the AM process.

Stability of nitrides

Similarly, for nitrides decomposition the following equation is valid:

$$\frac{2}{y}M_xN_y = \frac{2x}{y}M + N_2 \tag{9}$$

With M denoting the metal and M_xN_y the nitride.

The constant of equilibrium for this reaction can be derived as previously. It is interesting to plot the Gibbs standard free energy change versus temperature for different metal-oxide and metal-nitride systems, to study their relative thermodynamic stability, see Ellingham diagrams in Figure 7 and Figure 8. The standard Gibbs free energy of formation of oxides in general appears significantly lower than that of nitrides for the alloying elements of interest in this study (Fe, Cr, Mn, Si, Ti, Al). This suggests that oxides will more readily form than nitrides.

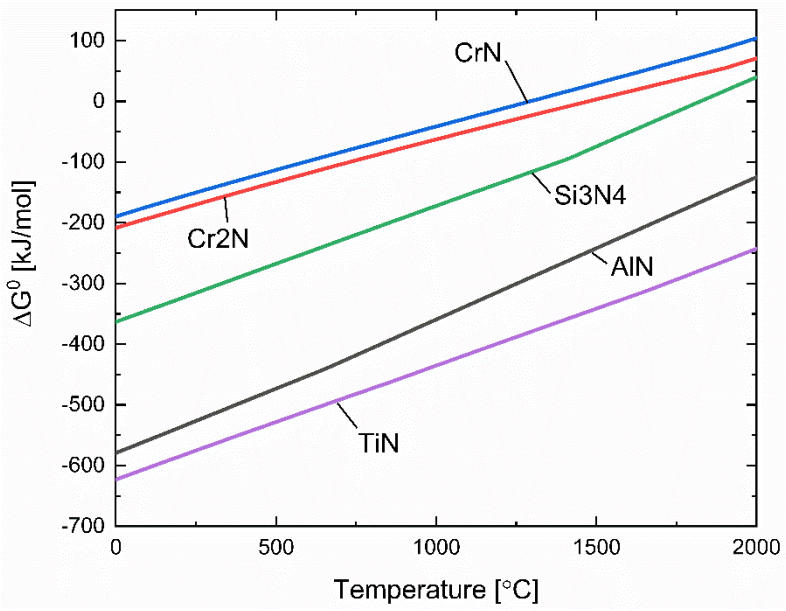

Figure 7: Ellingham diagram illustrating the thermodynamic stability of selected nitrides (plotted with HSC Chemistry).

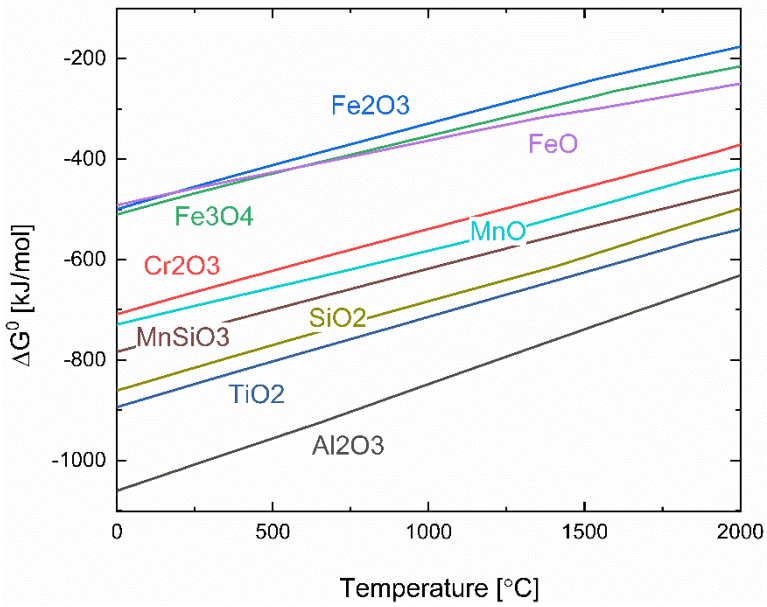

Figure 8: Ellingham diagram illustrating the thermodynamic stability of selected oxides (plotted with HSC Chemistry).

d. Effect on the process stability and resulting material properties

A few studies highlight the possible effect of the residual oxygen in the processing atmosphere on the produced material. For example, Li *et al.* [37] showed that when reducing the oxygen content from 2 % to 0.1 %, the balling phenomenon for 316L stainless steel can be avoided. Balling occurs when the laser melted track is discontinuous and appears as consecutive balls. They studied its appearance on the top layer of produced samples and single laser scan experiments. This was attributed to the oxidation of the melt pool surface and the further worsening of the wettability upon higher oxygen partial pressure. Still, the considered oxygen levels in that study (in 2012) are higher compared to actual systems capabilities nowadays. More recently, and in a similar manner, Dietrich *et al.* [6] highlighted that the surface roughness of $AlSi_{10}Mg$ is affected by the residual oxygen content. The authors showed that the lower oxygen content in the process atmosphere, the rougher the side surface is obtained. These studies stress that oxygen plays a significant role upon the melt pool dynamic and oxidation.

To the author´s knowledge, the effect of nitrogen content in the atmosphere on the nitride formation or nitrogen pick-up has not been reported in the context of L-PBF, even though its partial pressure is greater than that of oxygen under the standard processing conditions.

2.3.5. Summary

Figure 9 gives an overview of the effect of different phenomena involving the gas during the L-PBF process, mentioned above. The material outputs are the different properties of the material that can be characterized and that are influenced by the overall process parameters and more specifically the gas inputs.

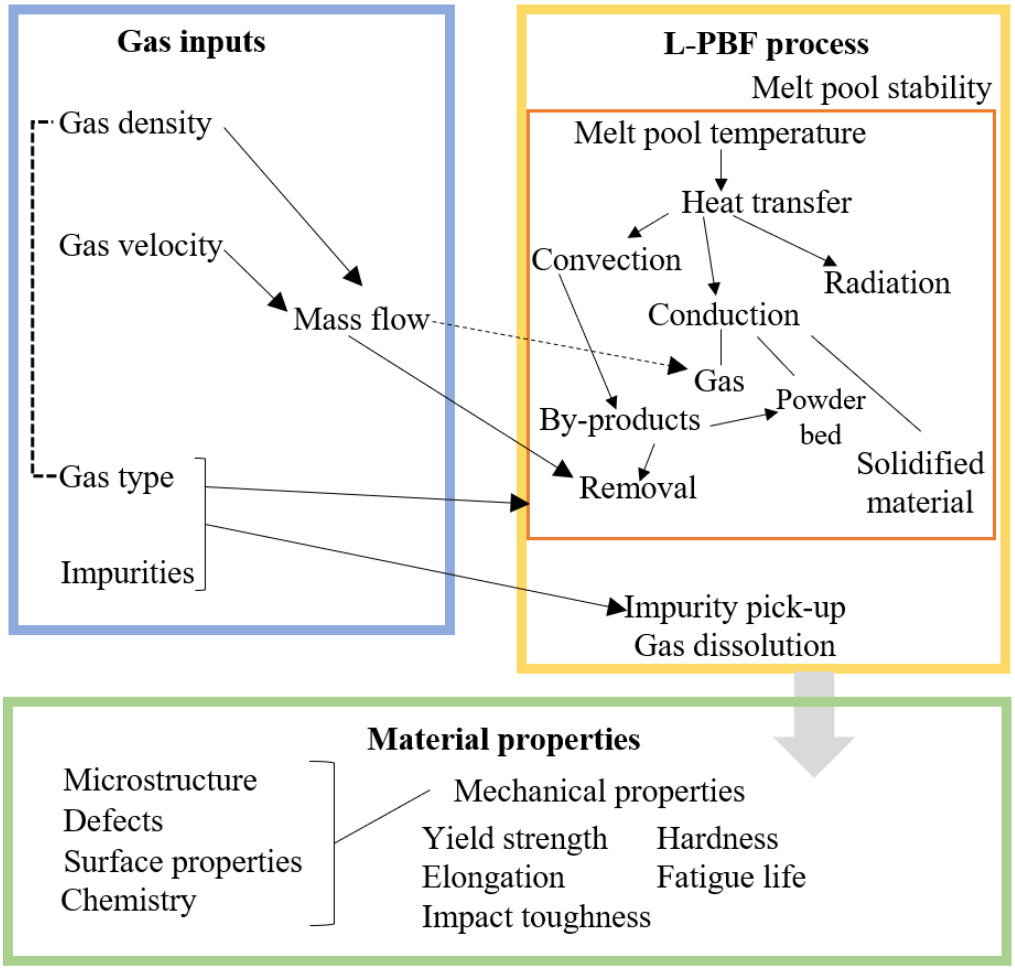

Figure 9: Overview of the gas inputs for the L-PBF process and the material outputs.

2.4. Stainless Steel 316L by L-PBF

Stainless steel 316L is among the most processable and robust alloys for L-PBF today. At least 17 wt. % of Cr ensures the formation of a stable protective oxide layer and thus a good resistance to corrosion. Its fully austenitic (γ) face centered cubic (fcc) structure is retained from room temperature up to its melting point (about 1450 °C), thanks to the stabilizing effect of Ni, present in sufficient levels (at least 12 wt. %). Besides, C and N are also strong austenite stabilizers, even in low quantities. As interstitials, they provide significant solid solution strengthening.

Stainless steel 316L is a carbon lean grade (which is specified by the “L”). It was developed to tackle weldability issues. As carbon may diffuse and combine with Cr to form carbides, lowering the local

corrosion resistance and causing intergranular corrosion. Other elements, such as Cr, Si, Mo, will tend to promote ferrite formation (δ or α).

2.4.1. Powder

As highlighted by Hryha *et al.* [38], the production techniques for 316L stainless steel powder are well established. Typical powder grades produced by gas atomization feature high purity surface, with minimum presence of oxide particulates, see Figure 10a and Figure 10b. Typically a thin uniform iron oxide layer of a few nanometres thickness covers most of the metal particle surface. When used for L-PBF, oxide particulate features rich in Cr, Mn and with traces of Si develop on the surface of the particles, see Figure 10c and Figure 10d.

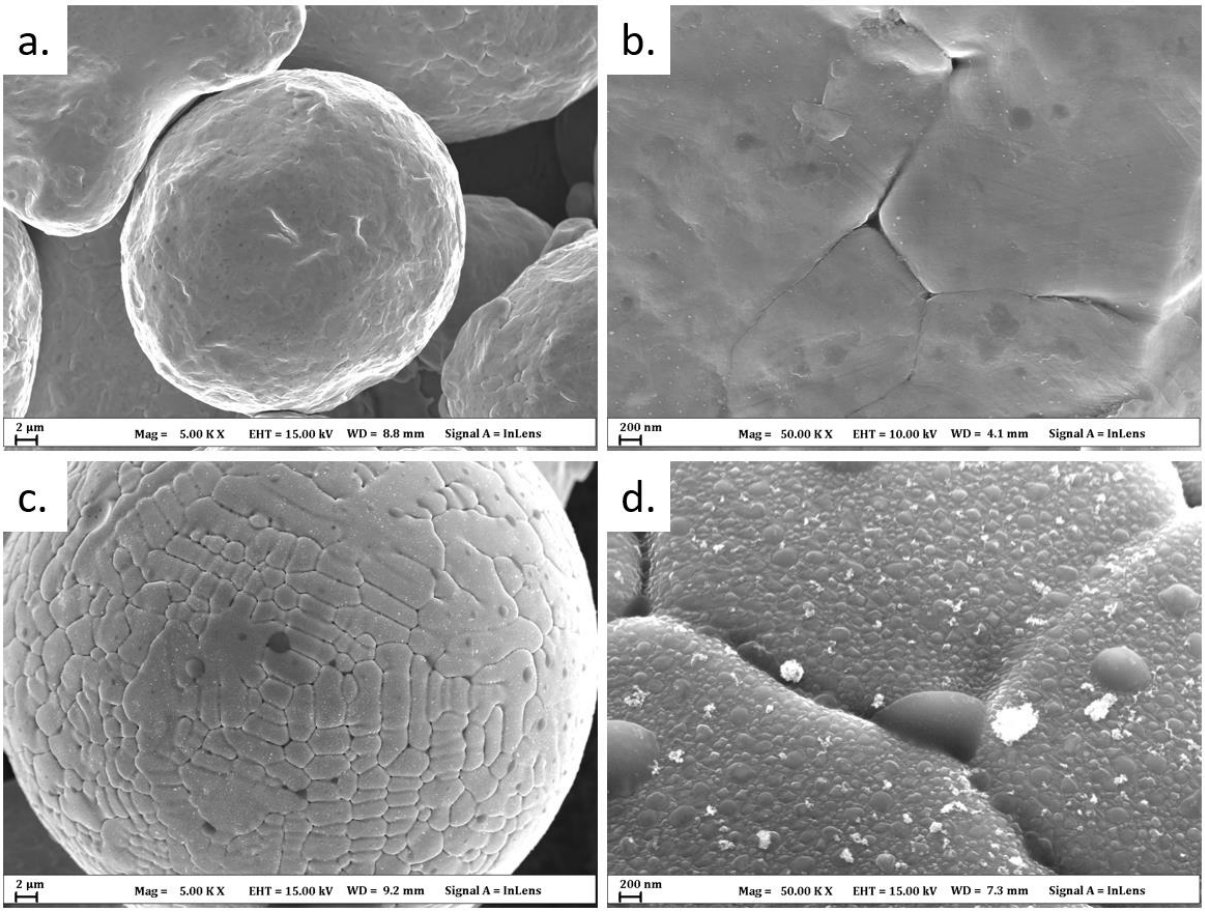

Figure 10: (a, b) Virgin 316L stainless steel powder; (c, d) 316L stainless steel powder recycled under nitrogen. Author´s experimental results.

2.4.2. Solidification and microstructure

As explained in Section 2.3.1, the powder will be melted by the laser beam, characterized by small focus spot (about 80 to 100 µm). The melt pool is heating and cooling extremely fast, owing to the small interaction volume and the short interaction times. The brief and repeated exposition to the laser will introduce high internal stresses and affect diffusional processes, such as precipitation, phase transformation and grain-growth. As a result, the material will exhibit a refined microstructure, very different from the ones obtained from casting or forging [39].

Figure 11 displays the typical microstructure observed for stainless steel 316L produced by L-PBF. Several melt pool boundaries of light contrast can be distinguished. As highlighted by Leicht *et al.* [40], large columnar grains aligned along the building direction (Z) contain several of these melt pool boundaries. This is consistent with the nucleation and epitaxial growth of the solid phase along the

steepest temperature gradient direction [41], [40] at the solid-liquid interface, with the solid being the previously formed grains.

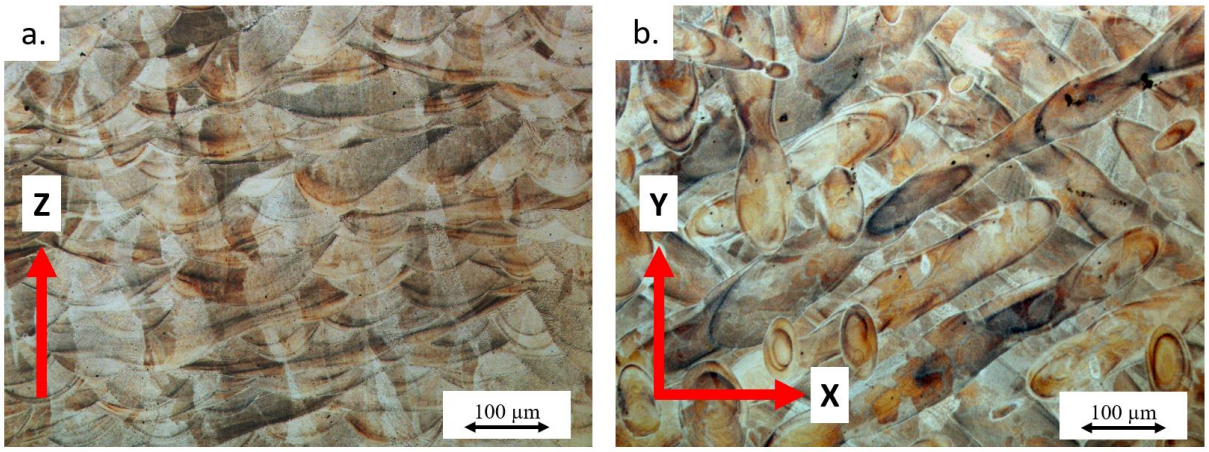

Figure 11: Optical micrographs of the etched microstructure of stainless steel 316L produced by L-PBF: a. along and; b. perpendicular to its building direction. Author´s experimental results.

A cellular structure is typically obtained inside the grains, see Figure 12. Sub-micron sized cells, also called sub-cells, are observed and are relevant of the L-PBF high cooling rates, which govern the spacing between the microstructure constituents upon solidification. The cells appear in different sizes, depending on the local cooling rate and their orientation with respect to the building direction. As shown by Zhong *et al.* [42], dislocations and hence micro-stresses accumulate at the sub-cell boundaries to which Mo is found to be segregated. They also identified some nano-sized Si rich inclusions at the sub-cell boundaries. Stacks of these sub-cells form colonies that grow through the melt pool boundaries, as reported by Krakhmalev *et al.* [43].

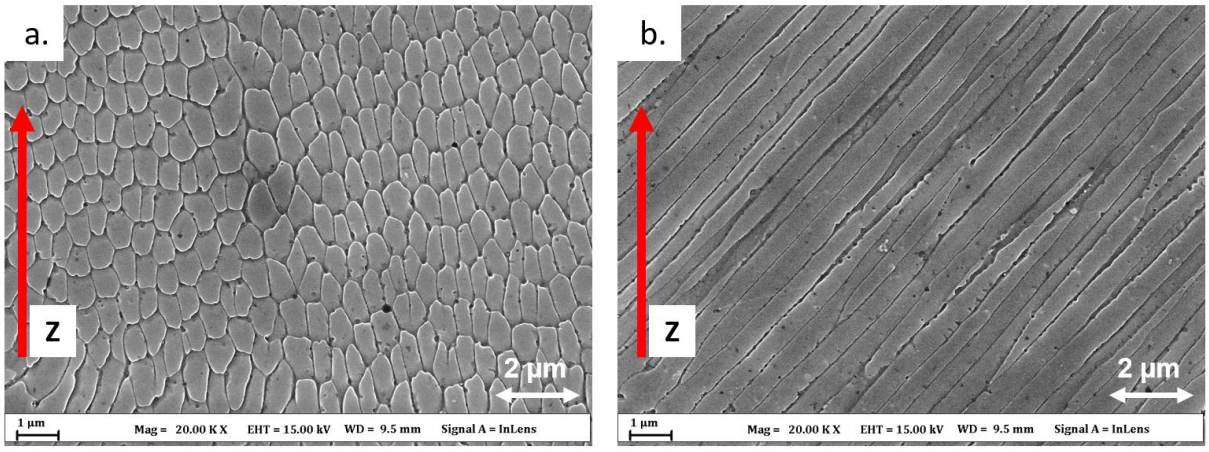

Figure 12: SEM micrograph of 316L stainless steel along its building direction highlighting a fine cellular microstructure of different orientation. Author´s experimental results.

The L-PBF high cooling rates ensure that the produced material is fully austenitic, and that no sigma phase is formed.

2.4.3. Properties

Melt pool boundaries, grain boundaries and cell boundaries contribute to the tensile strength of the produced material at full density. The cell boundaries are considered as the most important feature. Besides, the defects generated during the process reduce the material performances. Defects exist in various forms. Among them, pores can come in different shapes and sizes depending on their origin. Small spherical pores could arise from the gas entrapped within the powder during gas atomization. Gas pores may also come from gas species which could not dissolve within the material, such as argon,

and/or which did not have time to diffuse to the melt pool surface because of the high cooling rates. More irregular pores can be observed. The latter are commonly called lack-of-fusion defects and arise from too low energy input to create a proper material melting and bonding with the previously deposited material. Lack-of-fusion defects may derive from the not optimized parameters, presence of stable oxide layers, or oxidized powder particles, etc. Other flaws can be distinguished such as cracks, inclusions, incompletely melted particles, etc.

The fine microstructure produced enhances the strength of the material, comparable or even better to that obtained by conventionally processed material like casting. The elongation is also quite comparable. In addition, the as-built material is characterized by some anisotropy in properties. The vertically built samples will exhibit slightly lower strength and higher ductility [44]. Table 2 lists the mechanical properties reported by the manufacturer of the machine used in this study.

Table 2: Mechanical properties of as-built 316L stainless steel parts reported by the machine manufacturer EOS GmbH [44]

Ultimate Tensile Strength Vertical (Z)	540 ± 55 MPa
Ultimate Tensile Strength Horizontal (XY)	640 ± 50 MPa
Yield Strength Vertical (Z)	470 ± 90 MPa
Yield Strength Horizontal (XY)	530 ± 60 MPa
Elongation Vertical (Z)	50 ± 20 %
Elongation Horizontal (XY)	40 ± 15 %

2.4.4. Effect of nitrogen and oxygen

Nitrogen has been extensively added to austenitic stainless steels to benefit from its austenite stabilizing effect, limiting the formation of martensite at low temperatures and that of ferrite at high temperatures. Abundant and economical, it is also used for its ability to retard carbide formation and growth, and thus limiting sensitization. Around World War II, the shortage of nickel supported the research on substituting it by nitrogen to stabilize austenite, resulting in the AISI 200 series.

The nitrogen solubility in 316L stainless steel depends on the presence of other alloying elements, which affect its activity coefficient. Some elements, such as Al, Cr, Mn, Mo, Nb, Ta, Ti, V, and W, tend to decrease its activity, raising its solubility; while other will have the opposite effect such as B, C, Co, Cu, Ni, P, Si, and Sn. Because of the high affinity of Cr for N and its high Cr content, stainless steel 316L is likely to pick up some nitrogen.

According to Jiang *et al.* [45], the nitrogen solubility in molten 316L stainless steel follows Sievert´s law for nitrogen partial pressure not greater than 1 atm. In other words, for such pressures, the solubility of nitrogen is proportional to the nitrogen partial pressure above the melt pool. However, the authors also highlighted that upon higher pressure and higher concentration of alloying elements, Sievert´s law is not valid anymore, and nitrogen solubility is impaired. They also showed that while the nitrogen solubility increases with temperature for pure liquid iron, molten alloys containing Cr and Mn will behave differently.

The nitrogen can also dissolve in solid 316L stainless steel. Similarly as for molten steel, its solubility will depend on the temperature. Woo *et al.* [46] highlighted that the nitrogen solubility decreases for increasing temperature within the austenitic region. Therefore, more nitrogen may be dissolved upon low cooling rates. One should stress that the material produced under L-PBF will experience both high temperatures and cooling rates, which may in turn limit the dissolution of nitrogen.

The effect of nitrogen dissolution on the material properties will depend on the amount of nitrogen picked-up and its presence in the solution or as a nitride. As interstitial elements, small elements like nitrogen (or carbon and boron) increase the yield strength by the lattice expansion of the austenite. If the nitrogen pick-up is important, nitrogen may be supersaturated and precipitate with chromium to form Cr_2N nitrides. Finely dispersed, the precipitates may contribute to the strengthening. However, they are

likely to be detrimental to the alloy corrosion resistance, as the formation of nitrides will lead to a depletion of chromium within the austenitic matrix.

In addition, the rate of nitrogen absorption occurring through diffusion at the powder surface or melt pool will be reduced by the presence of nitrides or oxides. Indeed, Figure 8 shows that oxides rich in Si and Mn will be stable at high temperature. This is a well-known phenomenon, tackled in powder metallurgy by controlling the dew point during sintering. Indeed, by lowering the dew point, surface oxides may be removed, and nitrogen absorption enhanced. This accounts for the increase in nitrogen absorption upon cooling when using low dew point sintering atmospheres [47].

The solubility of oxygen in 316L stainless steel is relatively low compared to that of nitrogen. This is mainly attributed to the high affinity of elements such as Cr, Mn or Si to oxygen. The latter tend to form secondary phase oxide inclusions. Kitchener *et al.* [48] estimated the solubility of oxygen in austenite to be about 30 ppm. Above 30 ppm, oxygen is assumed to be present in secondary phases. More recently, Cooper *et al*. [49] highlighted that the strength of 316L stainless steel produced by Hot Isostatic Pressing (HIP) is not imparted for oxygen content below 200 ppm. For higher oxygen levels, Cr_2O_3 and MnO inclusions act as preferential sites for the nucleation of micro-voids during plastic deformation. Lou *et al.* [50] draw similar conclusions while studying the impact toughness of HIP 316L stainless steel produced by L-PBF. They showed that the fully recrystallized material exhibited randomly distributed semi-spherical oxide inclusions rich in Si and Mn within the grains and at the grain boundaries. They report an average size of 300 nm for these secondary phases. Their study of fracture surfaces highlighted the recurrent presence of the oxides within dimples. These oxides are held responsible for facilitating the onset of failure. In addition, as explained by Zhang *et al*. [51], the formation of Mn and Si oxides may reduce significantly their contribution as solid solution strengtheners, impairing the strength and ductility of 316L stainless steel.

2.5. Ti-6Al-4V by L-PBF

Ti-6Al-4V is an (α+β) alloy, likely to be the most commonly used titanium alloy, as it accounts for about 45 % of the total weight of the produced titanium alloys and more than 80 % of the titanium alloys employed in the aerospace industry. In aeroengines it is used to produce parts of the fan and compressor section where temperatures do not exceed about 350 °C [52]. It offers a high strength-to-weight ratio as well as good workability and weldability. Therefore, it has been identified as a good candidate for L-PBF adoption early-on and is now one of the established alloys processed by this manufacturing route.

Pure titanium is an allotropic element, *i.e.* it can be found in more than one crystal structure. At room temperature, it exhibits a hexagonal close packed (hcp) structure, the so-called alpha (α) phase. Above 888 °C, titanium transforms to a body centered cubic (bcc) crystal structure, referred to as the beta (β) phase. The α to β transition temperature, called β-transus temperature, is dependent on the addition of alloying elements. Therefore, alloying elements are divided into α stabilizers when they elevate the β-transus temperature (such as the substitutional Al, and the interstitials C, O and N), and β stabilizers when they lower it (for example V, Mo, Nb, Fe, Cr, Ni, Co, Cu, etc.), and finally, solid solution strengtheners which do not significantly affect the β-transus temperature (like Zr and Sn).

Upon quenching from the β phase, martensitic phases may precipitate (α′and α′′ phases). The α′ phase has a hcp structure like the α phase but has the same composition as the parent β phase. The α′′ phase has an orthorhombic structure. The type and amount of martensitic phases precipitating upon quenching depends on the composition of the parent β phase. If a β phase with about 10 ± 2 % of vanadium is quenched from temperatures about 750 to 900 ºC, α′′ phase precipitates. Upon higher solution treatment temperature, the vanadium content in the β phase is reduced and the α′ phase precipitates upon quenching. Besides, the metastable ω phase (simple hexagonal) can appear as nano-sized precipitates

from retained metastable β phase upon ageing around 400 to 500 ºC. Intermetallic phases can also be found: the α_2 phase (Ti_3Al) and γ phase (TiAl).

2.5.1. Powder

As emphasized by Hryha *et al.* [53], titanium has a high affinity to oxygen and because of the high surface area of the powder, the formation of a passivation oxide film on the surface of the Ti-6Al-4V powder is certain. As shown by Figure 6, titanium oxide has a high stability and thus the driving force for oxidation is considerable. The oxide film provides with proper passivation properties. Still, it is subjected to changes in thickness and composition depending on the atmosphere and temperature it is exposed to. The authors reported the presence of a homogeneous layer of TiO_2 (rutile) of a few nm. Within this rutile layer, they reported the presence of secondary phases rich in aluminium (Al_2O_3, corundum). This result was explained considering the decomposition of aluminium titanate (Al_2TiO_5) formed a high temperature during atomization into rutile and corundum.

2.5.2. Solidification and microstructure

Figure 13 displays the typical microstructure of Ti-6Al-4V produced by L-PBF. Yang *et al.* [30] showed that such microstructures are mainly martensitic (α´). Using transmission electron microscopy (TEM), they also identified a high density of dislocations and very fine retained β platelets and the Burger orientation´s relationship was verified. Using scanning electron microscopy (SEM), a hierarchical microstructure can be observed consisting of thick primary α´ lamellas, and finer secondary and tertiary lamellas, see Figure 13. The latter is generally observed when the material is subjected to repeated cyclic heat treatments. The thick primary lamellas are known to be observed across the entire parent β grains. The secondary lamellas are finer and are mainly observed parallel or perpendicular to the primary lamellas.

The work of Yang *et al.* [30] brings deeper understanding of the formation of this microstructure. When the material experiences peak temperatures above the liquidus temperature, the previously existing microstructure is fully disturbed and the liquid phase forms. Upon cooling below the solidus temperature, the transformation of the liquid to the β phase will occur rapidly. When the temperature reaches below the β-transus temperature, the microstructure is composed of large columnar β grains. Because of the high cooling rate and limited atomic diffusion, the β to α transformation is hindered. Upon further cooling to temperatures below the martensite start temperature (M_S), primary α´ lamellas precipitate at the parent β grain boundaries. This is accompanied by the generation of dislocations to release stresses and accommodate the martensite formation. As the already deposited material experiences the reheating cycles due to the deposition of subsequent layers, it will experience peak temperatures between the solidus and liquidus temperatures. As a result, the primary α´ lamellas will transform to the β phase, while a part of the β phase transforms to liquid phase, so that the liquid and β phase coexist. The authors suggest that some dislocations may remain within the residual β phase and act as nucleation sites for primary α´ lamellas upon cooling. Upon cooling, the liquid phase transforms to the β phase again (below the β-transus) and to primary α´ lamellas (below M_S), accompanied with the formation of additional dislocations. The residual β phase (not transformed to primary α´ lamellas) will transform into another type of martensite which is finer: the secondary α´ lamellas together with dislocations again. After several layers have been deposited, the material will experience thermal cycles of reduced peak temperatures, between the β-transus and the solidus temperatures. Therefore, only solid-state phase transformations occur. Upon heating, all martensite transforms to β phase, while some dislocations are conserved. Upon cooling, the residual dislocations trigger the nucleation and growth of the primary and secondary α´ lamellas. Finally, after a given number of deposited layers, the material will only experience reheating temperatures between the β-transus and the M_S temperatures. In turn, some of the previously formed lamellas decomposes to metastable β phase with residual dislocations, while the conserved α´ lamellas may be subjected to some coarsening. Upon cooling the β phase will transform to finer lamellas with dislocations, *i.e.* tertiary lamellas. Upon further reheating below Ms, most of the previously formed lamellas will be retained and may experience some little coarsening.

A small amount of martensite may transform to unstable β phase with high density of dislocation. The latter may transform to even finer lamellas.

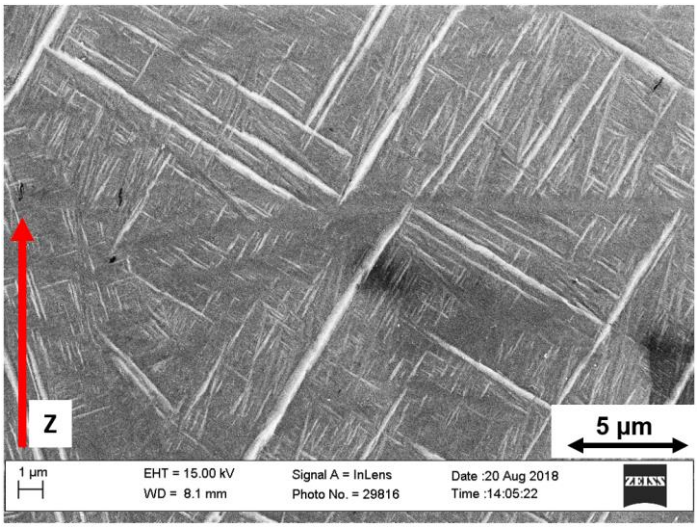

Figure 13: SEM micrograph of Ti-6Al-4V along its building direction.

2.5.3. Properties

Table 3 lists the mechanical properties reported by the manufacturer of the machine used in this study. High strength and poor ductility are generally reported and attributed to the microstructure observed in Figure 13 [54]. The hierarchical lamellar structure impedes the movement of dislocations and thus the onset of plasticity. As explained by Simonelli *et al.* [55] and observed in Figure 13, the α′ lamellas do not form colonies of lamellas sharing the same orientation, so that the effective slip length is limited to single α′ grains. As highlighted by Table 3, the produced material is characterized by some anisotropy. Qiu *et al.* [54] emphasized the role of the parent β grains boundaries for the fracture mechanisms. It was also reported that the absence of colonies together with a weak texture of the α′ (or α) phase, resulted in intergranular fracture along the parent β grain boundaries.

Table 3: Mechanical properties of as-built Ti-6Al-4V parts reported by the machine manufacturer EOS GmbH [56]

Ultimate Tensile Strength Vertical (Z)	1240 ± 50 MPa
Ultimate Tensile Strength Horizontal	1290 ± 50 MPa
Yield Strength Vertical (Z)	1120 ± 80 MPa
Yield Strength Horizontal	1140 ± 50 MPa
Elongation Vertical (Z)	10 ± 3 %
Elongation Horizontal (XY)	7 ± 3 %

2.5.4. Effect of nitrogen and oxygen

Upon increasing temperature, dissolution of the oxygen in the matrix starts and hence the oxide layer formed on Ti-6Al-4V is likely to lose its passivation properties and allow oxygen to dissolve. Oxygen and nitrogen are α stabilizers; increasing oxygen and/or nitrogen raises the β-transus temperature. They occupy the octahedral interstice of the α phase, so that an increase in dissolved oxygen or nitrogen leads to an increase of the lattice strain and thus of the lattice parameter ratio c/a. This reduces the number of slip planes of the α phase. This solid solution strengthening is observed by increased hardness and strength and limited ductility.

Oxygen is also known to promote martensitic transformations by increasing the martensitic transformation temperature [57]. The appearance of the martensitic phases (α′, α′′) is generally accompanied by an increase in strength but reduction in ductility. Oxygen is also believed to stabilize the intermetallic α_2 phase which also causes embrittlement [57], [58].

Nitrogen gas has been investigated to enhance surface properties of titanium alloys, by the so-called gas nitriding technique where nitrogen is introduced in the outer layers of components [59]. The diffusion of nitrogen is enhanced by increased temperatures (generally below the β-transus temperature), resulting in formation of nitrides at the surface. Hard layers of a few microns thicknesses are typically produced exhibiting a characteristic golden yellow aspect. In addition, the titanium nitrides exhibit higher oxidation resistance than the α phase, because of the strong interaction between titanium and nitrogen that reduces the thermodynamic activity of titanium as well as low solubility of oxygen in the TiN. They also act as diffusion barrier against oxygen that can be present in the gas [60]. Still, Figure 8 shows that oxides rich in Al and Ti will more readily form than nitrides.

Chapter 3: Experimental Methods

3.1. Materials and sample preparation

3.1.1. Stainless steel 316L

In this study, parts were produced by L-PBF using gas atomized stainless steel 316L powder as feedstock. Its particle size distribution (PSD) was between 20 and 53 µm, measured using a *CAMSIZERX2* (*Retsch Technology*). Table 4 displays the chemical composition of the virgin powder used.

Table 4: Chemical composition of the powder feedstock

Elements	Content [wt. %]
Fe	Bal.
C	0.013
Cr	16.7
Mn	1.5
Mo	2.5
N	0.0718
Ni	12.4
O	0.0588
Si	0.7

L-PBF fabricated samples for metallography study were prepared following standard Struers metallographic procedures, *i.e.* cut, mounted in conductive resin, ground and polished. For microstructural characterization, samples were electrochemically etched in a 20 vol. % oxalic acid solution.

3.1.2. Ti-6Al-4V

Gas atomized Ti-6Al-4V powder of grade 5, with a PSD between 18 and 44 µm, was used during this study. Table 5 gives the composition of the initial feedstock.

Table 5: Chemical composition of the Ti-6Al-4V powder feedstock

Elements	Content [wt. %]
Ti	Bal.
Al	6.43
V	3.95
Fe	0.18
O	0.1338
C	0.02
N	0.0056
Y	<0.001

L-PBF fabricated samples for metallography study were prepared following standard Struers metallographic procedures, *i.e.* cut, mounted in conductive resin, ground and polished. For microstructural characterization, samples were chemically etched with Kroll´s reagent (92 mL water, 6 mL nitric acid, 2 mL hydrofluoric acid).

The powder samples for SEM and EDX were prepared by pressing a small quantity of powder between two soft aluminium plates of 5 by 5 mm and further mounted on a fixture using carbon tape.

3.2. L-PBF system

3.2.1.L-PBF machine

The L-PBF machine used is an *EOS M290* (*EOS GmbH*) equipped with a Nd:YAG laser of maximal nominal power 400 W, see Figure 14. The processing atmosphere is established by the simple purge technique. The gas purged out of the chamber is vented out. As the oxygen level decreases, the flushed gas starts to be recirculated. The latter will pass through the so-called recirculation unit consisting of different filtering elements, allowing to remove process by-products. The pump of the machine is then activated and generates the desired gas flow velocity. When the oxygen level is stable at or below 1000 ppm, and the other sensors values are consistent (*e.g.* build plate temperature, etc.), the L-PBF process can start.

As described in Section 2.1.2, the simple purge technique resembles a dilution of the impurities present in the process chamber. Thus, when processing under argon and reaching an average oxygen level of 1000 ppm, the theoretical residual nitrogen level is about 4000 ppm and thus the processing atmosphere should consist of about 99.5 % argon. Similarly, when processing under nitrogen, one can expect about 99.9 % of nitrogen.

The *EOS M290* machine also features an integrated nitrogen generator, producing nitrogen from compressed air. The machine operator can choose in the machine´s interface whether to use technical gas or the generator as a nitrogen source. When using the generator, slight changes apply. The gas recirculation will start earlier, and the process will be launched when 10 000 ppm of O_2 are detected.

Figure 14: The used L-PBF machine EOS M290 and the ADDvance® O2 precision to its right.

For the first part of the work focusing on 316L stainless steel, standard *EOS* parameters were used. The second part, focusing on Ti-6Al-4V, was conducted using the standard *EOS* parameters as a benchmark and further studying the effect of the different laser parameters, *i.e.* laser power, scanning speed, hatch distance and layer thickness.

Table 6 lists the gases employed in this study and their purity levels. These gases may have different densities. Therefore, it has been necessary to set the L-PBF machine to ensure the same gas speed with the different gases.

Table 6: Gases used in this study

Gases	**Purity**	**Process O2 threshold**
Argon 5.0	≥ 99.999 %	1 000 ppm
Nitrogen 5.0	≥ 99.999 %	1 000 ppm
Nitrogen from the internal generator	Could be from 95 % to 99.9 %	10 000 ppm
Helium 4.6	≥ 99.996 %	1 000 ppm
VarigonHe50 (50 % Ar + 50 % He)	≥ 99.996 %	1 000 ppm
VarigonHe30 (70 % Ar + 30 % He)	≥ 99.996 %	1 000 ppm

3.2.2. Monitoring equipment

- Oxygen monitoring

An external system was connected on the L-PBF machine to analyse and control the residual oxygen level at the powder bed during the process: the *ADDvance® O2 precision* (*Linde Gas*), see Figure 14.

The system samples about one L/min of gas from the gas outlet of the L-PBF machine. This sample is therefore representative of the atmosphere close to the powder bed and the melt pool. The sample is analysed and brought back to the gas recirculation loop of the machine. In addition, the "control" function permits to achieve an O_2 level set by the machine operator. This is achieved by comparing the set O_2 level to the measured gas sample, and adjusting a flow of incoming fresh inert gas.

The system is equipped with an electrochemical oxygen sensor. It features an anode, an electrolyte and a cathode. The reduction of oxygen occurs at the cathode, while the anode material (lead) is oxidized, see the following equations.

$$4e^- + O_2 + 2H_2O \rightarrow 4\,OH^- \quad (10)$$

$$Pb + 2OH^- \rightarrow PbO + H_2O + 2\,e^- \quad (11)$$

The choice of the anode material imparts no sensitivity to other organic or inorganic gases possibly present in the gas sample (*e.g.* hydrogen, nitrogen). Strong inorganic oxidizing species such as fluorine, are the only exception, although not likely to arise in the context of L-PBF.

The rate at which oxygen molecules reach the surface of the cathode is proportional to the oxygen concentration present in the sampled gas. This rate defines the electrical output of the sensor. This sensor was calibrated with the calibration gases of very accurate oxygen concentration (*i.e.* about 1 ppm error). The oxygen content of the calibration gas is chosen carefully with respect to the targeted O_2 level defined by the operator. In addition, the oxygen sensor output will vary with the total pressure of the gas sample. Indeed, following Dalton´s law of partial pressure, if the total pressure increases, the partial pressure of the constituent gases will increase correspondingly. This is tackled by a thorough calibration of the system at the proper pressure.

- Process snapshots

Pictures of the laser spot were taken using a Canon PowerShot SX50 HS camera placed in front of the process chamber and mounted on a tripod. The camera placement and settings were carefully kept unchanged. The exposure time was set to 1/20 seconds with an ISO speed of 800, without additional illumination of the area of interest. The focal length was 34 mm. Considering the investigated scanning

speeds and the exposure time, a picture collects light while the laser scans a length from 35 mm to 60 mm, which corresponds to several laser passes.

3.3. Analytical techniques

3.3.1. Light Optical Microscopy (LOM)

In this thesis study, a Leitz DMRX microscope was used to analyse the polished samples surface. The porosity level was further measured using a thresholding method of the image freeware ImageJ. Microstructural characterization was performed on the etched specimens.

3.3.2. Scanning Electron Microscopy (SEM)

Scanning electron microscopy (SEM) allows to achieve high resolution since it is not limited by the wavelength of visible light as LOM. In SEM, a source (W, LaB6 or field emission gun) generates electrons which are accelerated through several apertures to potential of several keV. The electron beam is then collimated and focused by different electromagnetic lenses along the electron column. The beam is further scanned over the sample´s surface. A high vacuum is necessary for this purpose.

As the focused electron beam interacts with the material, several signals are produced as secondary electrons (SE), backscatter electrons (BSE) and X-rays. Secondary electrons coming from the ionization of atoms can escape from depth in the order of 100 nm because of their low kinetic energy. They provide topographical contrast. Backscattered electrons originate from the elastic scattering of the primary electron beam. Highly energetic, the signal has a lateral resolution in the micron range. As the backscatter yield is proportional to the mean atomic number, the signal also provides composition contrast. X-rays are a result of electrons decaying to fundamental state after ionization. Their information volume corresponds to a lateral resolution in the range of 1 to 10 µm. They depend on the incoming electron beam energy and are characteristic of each element.

In this study, microstructure, powder surface and fracture surface were investigated using the signal from SE. The X-ray signal was used for qualitative chemical composition analysis by energy-dispersive X-ray spectroscopy (EDX). Characterizations were performed using a LEO Gemini 1550 microscope equipped with an energy dispersive X-ray analyzer X-max (Oxford Instruments Ltd.).

3.3.3. Chemical analysis

The inert gas fusion technique was employed to measure the content of oxygen, nitrogen and hydrogen in the investigated metallic materials. The material is placed into a high purity graphite crucible. The material in the crucible is heated up to 3000 °C in an inert gas stream. Upon fusion, the oxygen present in the sample reacts with the crucible to form carbon monoxide (CO) and carbon dioxide (CO_2); while the nitrogen and hydrogen from the sample are directly released as gas molecules. These combustion gases are taken by the gas stream to dedicated sensors [61].

The inductively coupled plasma optical emission spectroscopy (ICP-OES) was used to determine the content of carbon and sulphur of the studied samples. First, the samples are dissolved in an acidic solution. Then, upon exposition to a plasma, the dissolved sample is ionized. Finally, the ionized species emit light of specific wavelength, allowing their identification. Their concentration can be derived from the intensity of the emission [61].

3.3.4. X-Ray diffraction (XRD)

X-ray diffraction (XRD) is commonly used for phase analysis. The X-rays produced by the X-ray tube irradiate the studied sample. They are diffracted by the sample phases and finally entering a detector. The detector records the intensity of the diffracted X-rays as a function of 2θ (angle between the incident and the diffracted beam) through the movement of the tube or sample and detector. The phase

identification is conducted by relating the diffraction angle to inter-planar distances using Bragg´s law:

$$n\,\lambda = 2\,d\sin(\theta) \tag{12}$$

Where n is the diffraction order, λ is the wavelength of the X-ray beam, d is the interplanar distance and θ is the diffraction angle. The set of diffraction planes obtained can be compared to that of a powder standard database. An ideal powder has no internal stresses nor texture, and thus can be used to identify the latter in the studied sample.

In this study, XRD was used to identify phases of the produced Ti-6Al-4V material. The instrument used was a PANalytical X´Pert PRO diffractometer with Cu Kα radiation operated at 45 kV and 40 mA, located at Höganäs AB.

3.3.5. Mechanical testing

The Charpy impact samples were produced horizontally, net-shape according to the ASTM E23 specification [62]. They were stress relieved with the tensile specimens, removed from the baseplate and the V-notch was machined.

For 316L stainless steel, the tensile samples were built horizontally, net-shape according to the ASTM B925-15 standard [63]. Before the removal from the plate, the stainless steel 316L samples were stress relieved at 300 °C for 2 h. The heat treatment and testing were performed at Höganäs AB.

For Ti-6Al-4V, the tensile samples were built horizontally, near net-shaped. Tensile and impact specimens were stress relieved at 650 °C for 3h. Finally, the tensile samples were machined to satisfy the geometry of the standard DIN 50125 Form B.

Chapter 4: Results and Discussions

In this chapter, the results of the appended articles are concisely discussed. Through the appended articles, the gas topic is elaborated under different conditions, specific materials and processing parameters. Herein, an overview of the different gas problematics covered is given. Below, the attached papers are listed, as well as the sections under which they are discussed.

Paper I: "Effect of Argon and Nitrogen Atmospheres of Different Purities on the Properties of Stainless Steel 316L Parts Produced by Laser-Powder Bed Fusion" is addressed in Section 4.1 and in Section 4.2.1.

Paper II: "Effect of Helium - Argon Mixtures as Laser-Powder Bed Fusion Processing Atmospheres on the Properties of the Built Ti-6Al-4V Parts" is addressed in Section 4.2.2.

Paper III: "Effect of the Laser-Powder Bed Fusion Gas Density and Thermal Properties on the Produced Ti-6Al-4V Parts" is addressed in Section 4.1 and in Section 4.2.2.

4.1. Purity of the process atmosphere

316L stainless steel parts were produced under argon and nitrogen at monitored residual oxygen levels (at about 20 and 700 ppm O_2). The oxygen monitoring device showed that accurate residual oxygen levels can be achieved in comparison to the relatively unstable oxygen levels obtained in standard operating conditions. Still, for this order of magnitude of oxygen partial pressure, no significant differences are noted in terms of density, microstructure, phase distribution, composition, strength nor impact toughness for the built 316L stainless steel material. This suggests that the dissolution of nitrogen and oxygen is limited. It is evident that only part of the oxygen from the powder feedstock is transferred to the built material. This is likely to be attributed to the dissociation of the surface oxides during interaction with the laser source. Produced oxygen gas is taken away by the gas flow and partly oxidises process by-products. For example, vaporized metal gas on top of the melt pool is oxidised and is also removed by the process gas. Oxidation of the spatter and ejected hot particles is also taking place close to the melt pool and also contribute to the oxygen removal from the system by the process gas.

Upon processing under higher oxygen partial pressure with the internal nitrogen generator, an additional pick-up of 50 to 100 ppm O_2 is measured in comparison with the nitrogen atmospheres obtained from the technical gas. The higher oxygen content in this material did not result in significant strength reduction. No changes in microstructural features were identified as well. However, the impact toughness was reduced in comparison to that obtained under 20 ppm residual oxygen in argon and nitrogen.

Despite the oxygen pick-up, the nitrogen content seemed to remain relatively unchanged. This could be understood by comparing the thermodynamic stability of oxides and nitrides. Figure 7 and Figure 8 show that the standard free energy of formation of oxides, possibly encountered in this system, is much lower than that of the nitrides. In other words, it is likely that the formation of nitrides is hindered in favour of that of the oxides. In addition, the very short life-time of the melt pool and the rapid cooling do not allow nitrogen dissolution due to the kinetic reasons. Consequently, the reduction of toughness can hardly be attributed to the precipitation of nitrides.

To correlate the noted oxygen pick-up to the toughness reduction, fracture analysis of the tensile and impact specimens was conducted. The fracture surface of the tensile specimens featured the typical ductile features and micrometre-sized spherical oxides in larger cavities, see Figure 15. Good cohesion between oxide particles and the matrix assumes that these oxides are likely to be formed during the short time the steel is in its liquid state. Their composition and shape are very similar to the oxide features, observed on the initial metal particles´ surface, see Figure 10, but a significant increase in size is noted.

This suggests that these oxide inclusions may have nucleated from the oxide particulates on the initial powder surface and further grow in size during metal powder melting and resulted in agglomeration with the oxide features from powder surface on the top of the melt pool. To lower their surface energy, they become spheroidized. The examination of the fracture surfaces of the impact specimens revealed large deep dimples (up to 100 µm) for the material produced with the nitrogen generator, see Figure 16. These defects appeared aligned along the loading direction which is also corresponding to the building direction. Ridges were also observed within these dimples and suggest that these flaws are lack-of-fusion defects. Indeed, no spherical oxides like the ones observed on the tensile surfaces were found. It could be that the latter were larger in size and detached from the surface during the sample handling. It may also be that these defects originated from oxides of different morphology (*e.g.* plate-like or forming a thin layer on the previously solidified material) or from composition inhomogeneities that can affect the melting point of the material.

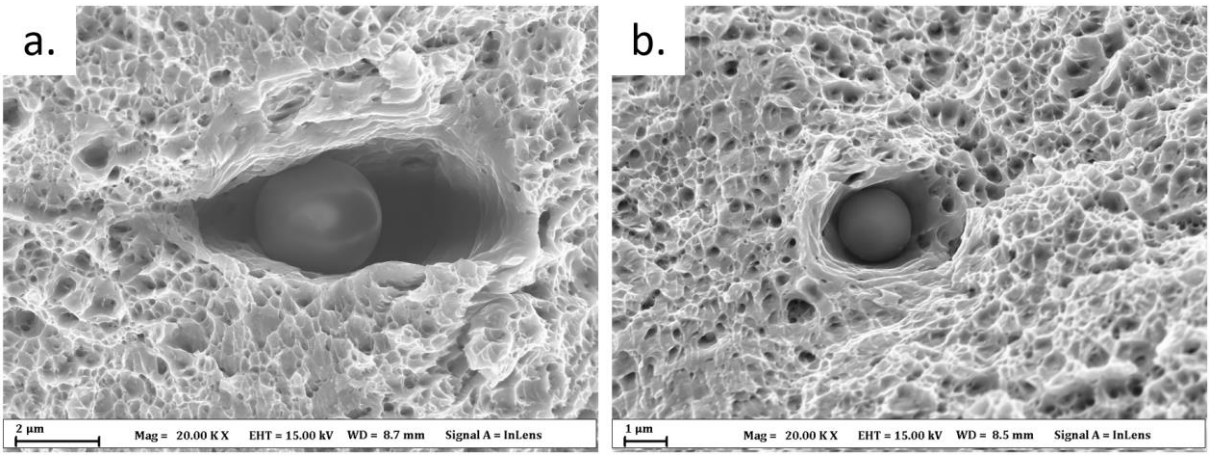

Figure 15: Examples of spherical oxides rich in Cr, Mn and with some traces of Si, commonly observed on the fracture surfaces of 316L stainless steel processed in argon (a.) and nitrogen (b.).

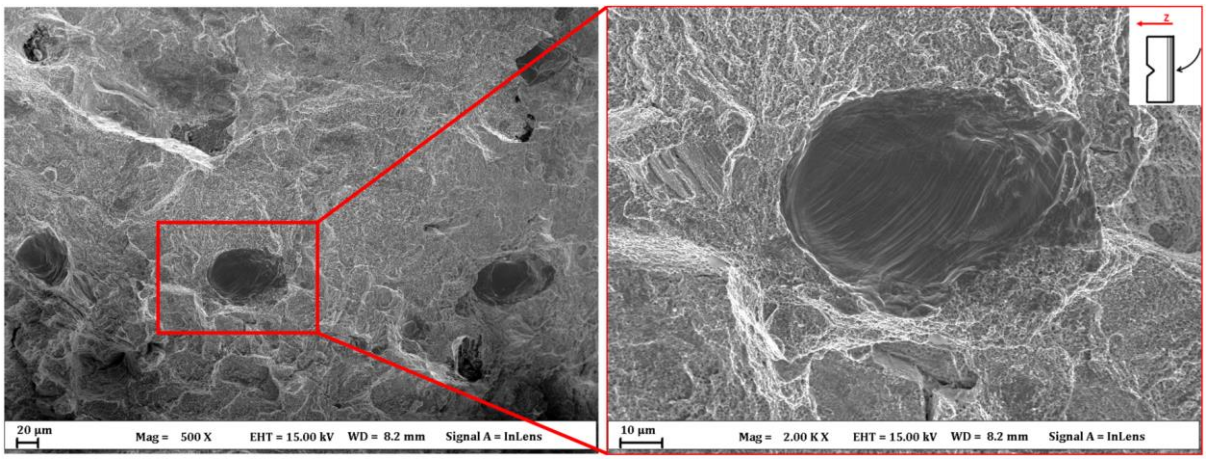

Figure 16: Fracture surfaces of the 316L stainless steel impact specimen produced with the nitrogen generator.

Finally, the kinetics for powder oxidation appeared to be enhanced when exposing it to higher oxygen partial pressure. The development of oxide particulates appearing dark in the SEM image, rich in strong oxide forming elements (Cr and Mn with traces of Si), was prematurely identified for the powder exposed to overheating and the atmosphere generated by the nitrogen generator. The enhanced powder particles degradation could explain the occurrence of lack-of-fusion defects on the fracture surface of impact specimens built with the nitrogen generator.

Compared to 316L stainless steel, Ti-6Al-4V is very sensitive to oxygen, as its main alloying elements (Ti and Al) have a very high affinity to oxygen and form particularly stable oxides, see Figure 8. In this

thesis, Ti-6Al-4V has mainly been employed to study the influence of helium processing, see Section 4.2.2. To assess the necessity to use an external oxygen monitoring system, a build job was conducted without it. It appears that the material produced as such was more porous and less homogeneous than under controlled Argon 5.0. Examples of the observed lack-of-fusion porosity are given in Figure 17. This trend is compatible with the recorded unstable oxygen level in standard conditions (*i.e.* 490 ± 401 ppm) in comparison with the monitored one (*i.e.* 98 ± 4 ppm). An additional pick-up of about 50 ppm oxygen was measured in comparison with the controlled one, which in turn didn´t affect significantly the material´s strength.

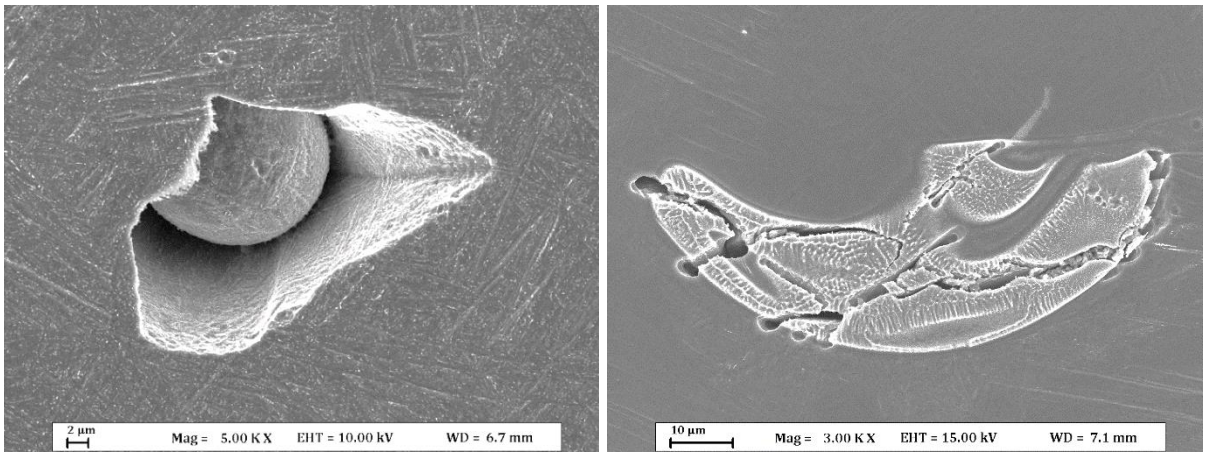

Figure 17: Lack-of-fusion defects observed for the Ti-6Al-4V material built without the external oxygen monitoring system.

The presented results aimed at raising awareness of the influence of the purity of the L-PBF atmosphere. The requirements on residual oxygen levels must be determined in accordance with the considered material grade. 316L stainless steel is a relatively robust alloy, not too sensitive to oxygen pick-up when processed by L-PBF, which is not much affected by oxygen levels below the usually used threshold of 1000 ppm O_2. For higher oxygen levels, the powder feedstock degrades, and the produced material dissolves some oxygen. More strict guidelines shall be specified for grades sensitive to oxidation such as Ti or Al alloys. Indeed, higher oxygen partial pressures may result in porosity and defects because of enhanced oxidation, even below the 1000 ppm O_2 threshold. Considering these conclusions, the study of the effect of the gas density conducted with Ti-6Al-4V was initiated by setting the oxygen level to 100 ppm, to limit the effect of the residual oxygen on the occurrence of lack-of-fusion defects.

4.2. Properties of the gas

4.2.1.The gas type

316L stainless steel powder was used to investigate the effect of the type of gas used for L-PBF on the built material properties by using high purity argon and nitrogen gas.

Even though the nitrogen levels in these two atmospheres are of different orders of magnitude, the chemical analysis of the produced parts did not indicate significant variation in nitrogen content for the produced parts. Only a slight increase of 50 ppm was measured for parts produced under nitrogen. In addition, the results highlight that all the nitrogen initially present in the powder feedstock is transferred to the built material.

On the one hand, the L-PBF process involves high peak temperatures which could promote the dissociation of the nitrogen molecules at the surface of the metal and thus the nitrogen pick-up. Besides, the solubility of nitrogen in liquid iron increases with the temperature. On the other hand, the exposition time of the powder bed to the laser radiation is of about 0.01 s for the used laser parameters. This results in the high cooling rates characteristic of the L-PBF process (10^5 - 10^7 K/s). This is likely to limit the

nitrogen dissolution, as the high cooling rate could be expected to inhibit the nitrogen dissolution. This is supported by the chemical analysis results. It could also be that the nitrogen dissolution is hindered by the presence of oxides on the molten metal surface.

The microstructures obtained using the two gases were observed using LOM and HR-SEM. The typical features resulting from L-PBF were observed, see Section 2.4.2. No differences between the cellular structures neither in terms of defect types nor amount were noted. Both processing atmospheres allowed to achieve high density material (at least 99.9 % dense). No nitrides were identified in either of the material. It should be emphasized that the observation of these nitrides depends on the sample preparation and the resolution of the characterization technique. For aged CrMnN austenitic steels (800 ºC for 30 minutes), Cr_2N nitrides of hundreds of nm have been reported in the literature and observed using SEM [64]. Smaller nitrides of a few tens of nm have been observed dispersed at grain boundaries using transmission electron microscopy (TEM) [64]. As displayed on Figure 12, the oxalic acid preferentially etches the sub-cell boundaries of 316L stainless steel. It has been shown that these sites are enriched in Mo [42], Cr and Si [65]. Since nitrides were not observed, it can´t be discarded that sub-cells boundaries could be a preferential site for nitride precipitation. Nitrides may be revealed using a softer etchant such as the Glyceregia reagent and conducting TEM analysis. Nitrides formation may also be highlighted by the reduction of the corrosion resistance of the material. Still, the obtained results suggest that the nitrogen is mainly present in solid solution within the austenitic matrix.

The XRD spectrum of nitrogen and argon processed 316L stainless steel (not included in the appended papers) revealed a fully austenitic structure with unchanged peak position, intensity and width. If the strengthening of 316L stainless steel by nitrogen in solid solution would be important, a shift in the diffracted intensity peaks may be observed because of the lattice distortion introduced by the nitrogen atoms.

The mechanical properties of both types of materials are similar and slightly above that obtained by conventional processing techniques. The nitrogen pick-up under nitrogen processing is probably too little to cause some significant strengthening. The consistent toughness for the different materials is attributed to the negligible nitride precipitation.

4.2.2.Density of the gas

Ti-6Al-4V gas atomized powder and gases ranging from pure argon to pure helium were employed to study the effect of the gas density on the L-PBF process (Paper II and Paper III). As described in the Introduction chapter, the gas density will affect the heat transfer as well as the drag force applied on the projections.

The process snapshots taken showed that the visible projections for similar laser parameters are different under argon and under helium, see Figure 18 and Figure 19. Both, the amount of projections generated, and their removal can be seen on those pictures. It seems that less projections are generated within helium and that their trajectories are straighter and shorter than under argon, see blue arrows. In red are circled projections that interact with the laser beam and appear incandescent as they interact with the laser during the camera exposure time. As the exposure time is relatively long (1/20 sec) and the scanning speed is of the order of 1 m/s, the light from a relatively significant amount of these incandescent particles can be captured. Such hot particles are more present under argon and observed at a larger distance above the interaction point. This highlights a higher production of these particles under argon. Besides, the laser spot appears larger and more saturated under argon. Using camera with higher frame rate may support this comparison.

It is interesting to put these results in regards with the work performed by Bidare *et al.* [20] on an in-house developed L-PBF setup. Their system is a small size pressurized chamber. Therefore, their study do not highlight the effect of the gas density on the drag force and thus on the particles removal. Still, the authors were able to stress that metal vapour flow escapes faster under helium, as helium is lighter

and has a lower kinematic viscosity than argon. The metal vapour flow is likely to cause significant defocusing of the laser by absorption, scattering and shadowing, and thus reducing the energy input. Their results suggest that argon promotes the accumulation of this vapour and possibly plasma at the melt pool.

Similarly, as observed in Figure 18 and Figure 19, Bidare *et al.* [20] observed greater amount of projections under argon. They attributed this generation to a greater melt pool temperature and metal vapour temperature under argon than under helium. This would be consistent with the large and bright laser spot observed under argon. Section 2.2 showed that the heat capacity rate is similar for argon and helium. Therefore, the temperature difference may be attributed to the lower thermal conductivity of argon.

In addition, it should be underlined that the drag force achieved by helium for the set speed was enough to remove the visible projections.

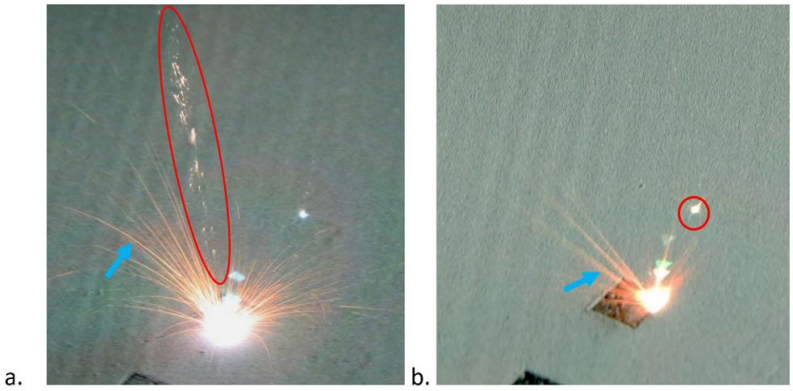

Figure 18: Process snapshots of Ti-6Al-4V under a. argon and b. helium.

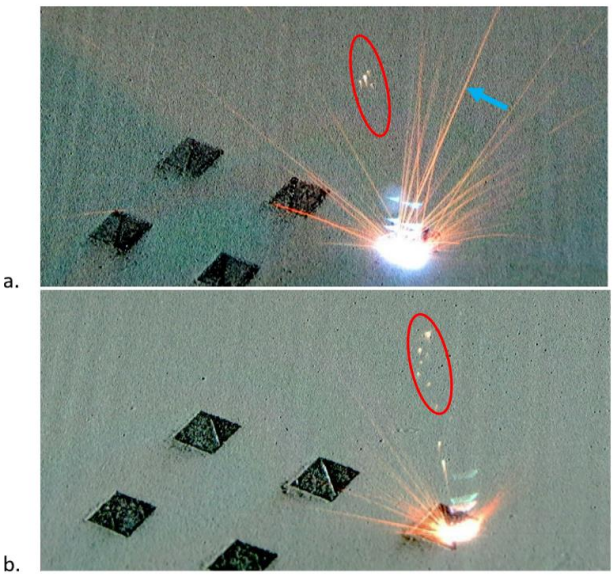

Figure 19: Additional snapshots of Ti-6Al-4V under a. argon and b. helium.

It would be interesting to perform similar process imaging for mixtures of argon and helium, to further identify a possible trend in the generation of projections with additions of helium. A mixture of argon and helium would offer an interesting trade-off of density and thus drag force, and thermal conductivity. In addition, one should verify if the observed effect of helium is confirmed with another powder material. Trying to optimize the gas speed for helium and its mixtures with argon to achieve enhanced heat capacity rate shall also be considered.

The achieved material density appears to also be influenced by the density of the gas. Paper II reports a decrease of the porosity of the produced material using helium for a processing window shifted towards larger layer thicknesses with respect to the standard EOS process. Paper III shows that high density is achieved within a processing window around the standard EOS parameters. Paper III also highlights that helium and its mixtures are interesting to increase the density of the produced material, using high scanning speeds and thus build rates. In Paper II, relatively large layer thicknesses (50 µm) were employed and thus the scanning speed was lowered (700 to 1200 mm/s) to achieve proper energy input. In Paper III, higher scanning speeds (1400 to 2400 mm/s) were used to investigate the effect of the gases upon high build rates.

The material produced and studied in Paper II was further analysed using XRD. Regardless of the processing atmosphere, no peaks for the bcc β phase were observed for the as-built material, which highlights the major presence of the α phase and possibly α´ martensite. In Paper III, the XRD spectrums obtained for argon, argon-helium mixtures and helium are quite dissimilar from each other, see Figure 20. While the argon and helium material are very similar to the one studied in Paper II, the spectrum measured for gas mixtures features low intensity broad α peaks, attributed to increased residual stresses. Upon stress relieving at 650 ºC for 3h, the α peaks in material produced in gas mixtures narrowed, highlighting the stress removal, see Figure 21. The resulting spectrum is very similar to that of pure gases, with the appearance of a low intensity $(200)_{\beta}$ peak. This peak was correlated to the SEM observations of finely dispersed sub-microns sized β precipitates.

As explained by Li *et al.* [66], residual stresses in L-PBF mainly arise from important temperature gradients and cooling rates. Therefore, it could be that the heat input is greater under argon-helium mixtures. As shown in Table 1, the mixtures offer an interesting trade-off of density and thermal conductivity. This may lead to proper removal of the process by-products as well as enhanced transfer of the laser energy to the material. This is also consistent with the reduced lack-of-fusion porosity obtained when processing under the gas mixtures. Since the mechanical testing was performed on the stress-free heat-treated specimens, the impact strength, tensile strength and elongation were comparable for the different gases.

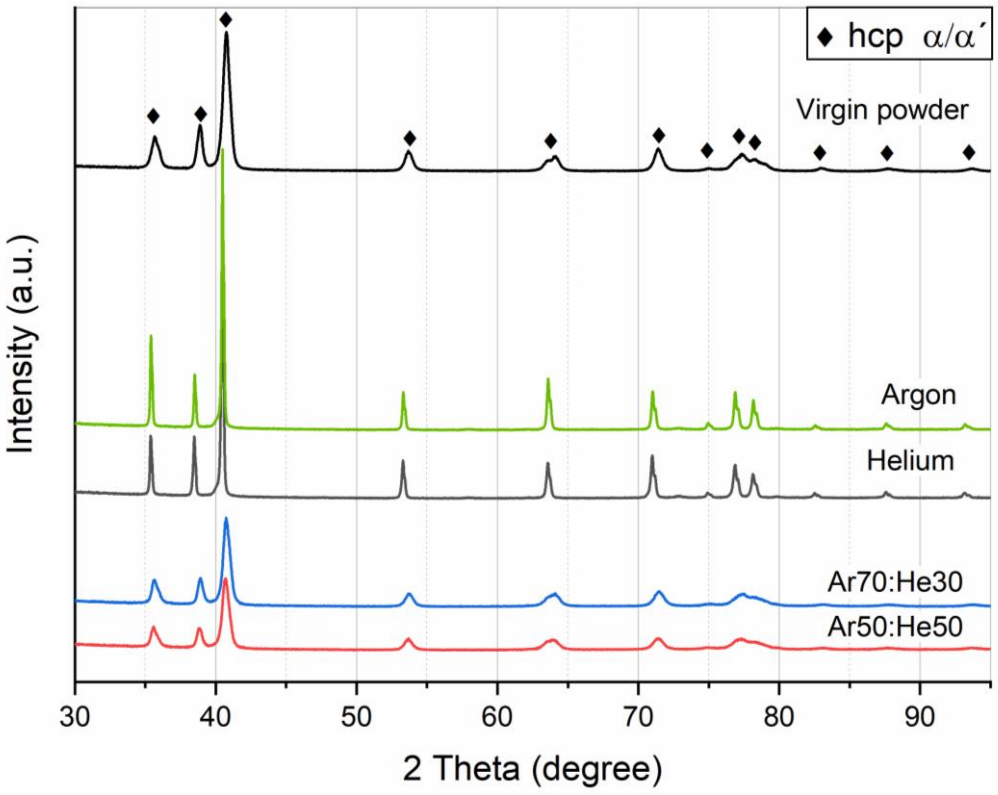

Figure 20: XRD spectrum of theTi-6Al-4V material produced under argon, argon-helium mixtures and helium (Paper III).

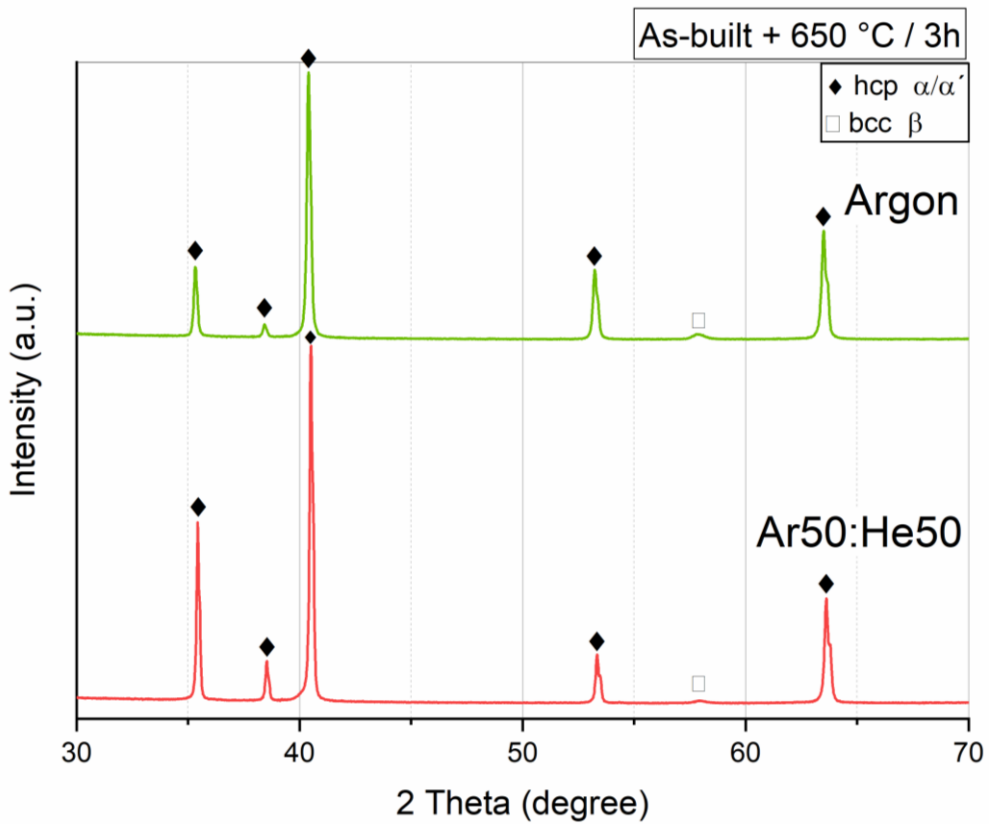

Figure 21: XRD spectrum of stress relieved Ti-6Al-4V materials (Paper III).

From Paper II and Paper III, in can be stated that the reduced porosity under helium is attributed to a better energy transfer from the laser radiation to the material. As highlighted by the process pictures, more projections are observed under argon, and the interaction area appears larger and more incandescent than under helium, suggesting that the melt pool is more unstable and that a lot of energy is consumed by interactions with the by-products. In addition, gas mixtures of intermediate gas density and thermal conductivity are likely to allow to enhance the density of Ti-6Al-4V parts. This may allow to further increase the productivity of the L-PBF process by using larger layer thicknesses and faster scanning speeds.

Chapter 5: Summary and Conclusions

The following conclusions can be drawn from the work presented in this thesis:

316L stainless steel is a robust alloy to process by L-PBF. Its mechanical properties are not significantly affected by the usual residual oxygen present in the process chamber (about 1000 ppm O_2) nor the gas type (argon or nitrogen). However, the study of Ti-6Al-4V highlighted a significant sensitivity to oxygen, which affects the porosity even within the 100 to 1000 ppm O_2 range.

Upon processing of 316L stainless steel with lower purity gas supply, such as a nitrogen generator, *i.e.* 2000 ppm residual O_2, risks related to powder degradation arise. The driving force for this oxidation lies in the difference in oxygen chemical potential between the surface of the metal particle and its core. This triggers the mass transfer of strong oxide forming elements such as Cr, Mn and Si and hence oxide features develop on the powder surface when the metal particles are heated in the oxygen-rich gaseous environment. During L-PBF, these stable surface oxides may be transferred to the material as inclusions or introduce lack-of-fusion defects. The reduction in the impact toughness of 316L stainless steel manufactured using lower purity of the process gas is likely to reflect the increased fraction of these defect sites.

Processing 316L stainless steel under high purity nitrogen did not lead to notable nitrogen dissolution and the material exhibited similar properties to that obtained using argon. This was attributed to the rapid solidification and the potential presence of oxide layer on the melt and solidified material surface, which limits the nitrogen dissolution and diffusion. Ensuring a proper control of the residual oxygen level and gas flow allowed to successfully implement the use of lighter gases – argon-helium mixtures – for the L-PBF of Ti-6Al-4V. The results clearly indicate that helium reduces the amount of observed by-process projections and thus minimises their generation and improves their removal. The use of gas mixtures appeared to be promising to enhance the input energy to the material and thus the density upon higher built rates. This was attributed to the positive balance of gas density and thermal properties offered by these gas mixtures.

Future work

The L-PBF trials with argon-helium mixtures were conducted on Ti-6Al-4V. The gas mixtures allowed to reduce the built material lack-of-fusion porosity. Consequently, the study of the effect of helium additions for other materials shall clarify the effect of the gas density and its thermal properties. 316L stainless steel is heavier than Ti-6Al-4V, therefore the same gases with the same flow characteristics shall result in different ability to remove projections. In addition, the thermal conductivity of 316L stainless steel is about two times higher than that of Ti-6Al-4V and will have a significant impact on the convection and melt pool stability. Besides, the effect of helium addition on the residual stresses could be further investigated by building cantilever structures which deform upon removal.

Since the gas ability to remove heat is dependent on its thermal properties and the mass flow, different gas flow properties shall be considered. One can expect that for the considered material, there is an optimal combination of helium content and gas flow to ensure a stable process upon higher build rates. The computational fluid dynamics modelling of this situation is likely to support experimental trials.

Effort should also focus on the evaluation of the gas effect on the melt pool stability. This could be done by attempting to correlate the process parameters (including laser and gas related ones) with the information collected by online melt pool monitoring systems. The result should aim at minimizing the generation of process by-products and their effect on the contamination of the built material.

Acknowledgments

First, I would like to thank my supervisors Prof. Eduard Hryha and Pierre Forêt and co-supervisor Prof. Lars Nyborg for giving me the opportunity to embark on this journey rich in learnings and encounters, and for their input and assistance through the work.

Gratitude goes to Linde AG and the Centre for Additive Manufacturing – Metal (CAM^2), supported by Vinnova, for supporting the framework within which this work has been conducted.

I am thankful to Sigurd Berg, Adj. Prof. Sven Bengtsson and Dr. Björn Skårman from Höganäs AB for their support with material testing.

Living in Sweden, Germany and Sweden again, allowed me to meet many interesting, helpful and caring individuals and forge links within and beyond these two countries. I express my gratitude to my colleagues working at Linde AG: Kai, Dominik, Sören, Andrés, Thomas, Jens, Sebastian, Jürgen, Bo. A warm word for the "AM ladies", Sophie, Tanja and Anja. My regards also go to Christoph Laumen, Michael Seys and Marc-Oliver Koerner. Special thanks are sent to Edward Feng for helping me with my visit to Beijing.

This Chinese trip wouldn´t have been the same without Eduard, Swathi, Mahesh, Dmitri and Johan (and that person sharing our dinner table), whom I also acknowledge for their scientific discussion. Among my "Swedish" colleagues, I would like to give a special thanks to the AM teammates for their active discussion and support: Alex, Hans, Dmitri, Eric, William, Michael, Marie, Masoud, and Lars; and for your everyday help, discussion and attention, Roger. I am also very grateful to Casey, Antonio, Philip, for their daily joyful and kind presence. I would like to acknowledge all my colleagues from the Department of Industrial and Materials Science.

Special thanks go to my friends, close-by or further away, to Léa and Maéva for their surprises, to Stefan for supporting and encouraging me.

Thanks to my parents, Joëlle and Jean-Jacques, and my brothers, Richard and Maxime, for your love and help, for supporting me from the distance and creating beautiful moments together.

References

[1] ASTM International, *F2792-12a - Standard Terminology for Additive Manufacturing Technologies*. 2013.

[2] I. Baturynska, O. Semeniuta, and K. Martinsen, "Optimization of process parameters for powder bed fusion additive manufacturing by combination of machine learning and finite element method : A conceptual framework," *Procedia CIRP*, vol. 67, pp. 227–232, 2018.

[3] "Siemens and E.ON reach milestone with 3D-printed burner for SGT-700 gas turbine," 2018. [Online]. Available: https://www.siemens.com/press/en/feature/2014/corporate/2014-03-3d-druck.php. [Accessed: 23-Jan-2019].

[4] W. Associates, "Wohlers Report 2017," 2018.

[5] D. M. Bauer, K. Dietrich, M. Walter, P. Forêt, F. Palm, and G. Witt, "Effect of Process Gas and Powder Quality on Aluminum Alloys Processed by Laser Based Powder Bed Melting Process," *Proc Int Solid Free. Fabr. Symp.*, pp. 419–425, 2016.

[6] K. Dietrich *et al.*, "Which Laser Parameters Influence the Oxide Formation and the Mechanical Properties of Laser Beam Melted (LBM) Parts," no. March, pp. 8–15, 2018.

[7] E. Almqvist, *History of Industrial Gases*. Boston, MA: Springer US, 2003.

[8] A. A. Clifford, R. Fleeter, J. Kestin, and W. A. Wakeham, "Thermal conductivity of some mixtures of monatomic gases at room temperature and at pressure up to 15 MPa," *Phys. A Stat. Mech. its Appl.*, vol. 98, no. 3, pp. 467–490, 1979.

[9] J. Trapp, A. M. Rubenchik, G. Guss, and M. J. Matthews, "In situ absorptivity measurements of metallic powders during laser powder-bed fusion additive manufacturing," *Appl. Mater. Today*, vol. 9, pp. 341–349, 2017.

[10] A. Simchi, "Direct laser sintering of metal powders: Mechanism, kinetics and microstructural features," *Mater. Sci. Eng. A*, vol. 428, no. 1–2, pp. 148–158, 2006.

[11] P. Fischer, V. Romano, H. P. Weber, N. P. Karapatis, E. Boillat, and R. Glardon, "Sintering of commercially pure titanium powder with a Nd:YAG laser source," *Acta Mater.*, vol. 51, no. 6, pp. 1651–1662, 2003.

[12] B. Dikshit and M. S. Bhatia, "Studies on Electron Beam Vapor Generation in PVD Processes," *BARC Newsl.*, no. 314, pp. 10–19, 2010.

[13] W. Pei, W. Zhengying, C. Zhen, L. Junfeng, Z. Shuzhe, and D. Jun, "Numerical simulation and parametric analysis of selective laser melting process of AlSi10Mg powder," *Appl. Phys. A*, vol. 123, no. 8, p. 540, 2017.

[14] Z. Li, M. Zeze, and K. Mukai, "Surface Tension and Wettability of Liquid Fe-16mass%Cr-S Alloy with Alumina," *Mater. Trans. JIM*, vol. 44, no. 10, pp. 2108–2113, 2003.

[15] Z. Li, K. Mukai, M. Zeze, and K. Mills, "Determination of the surface tension of liquid stainless steel," *J. Mater. Sci.*, vol. 0, pp. 2191–2195, 2005.

[16] A. Masmoudi, R. Bolot, and C. Coddet, "Investigation of the laser-powder-atmosphere interaction zone during the selective laser melting process," *J. Mater. Process. Technol.*, vol. 225, pp. 122–132, 2015.

[17] P. Shcheglov, *Study of Vapour-Plasma Plume during High Power Fiber Laser Beam Infl uence on Metals*. 2012.

[18] M. Aden, E. Beyer, and G. Herziger, "Laser-induced vaporisation of metal as a Riemann problem," *J. Phys. D Appl. Phys.*, vol. 23, pp. 655–661, 1990.

[19] P. Solana and G. Negro, “A study of the effect of multiple reflections on the shape of the keyhole in the laser processing of materials,” *J. Phys. D. Appl. Phys.*, vol. 30, no. 23, pp. 3216–3222, 1999.

[20] P. Bidare, I. Bitharas, R. M. Ward, M. M. Attallah, and A. J. Moore, “Laser powder bed fusion in high-pressure atmospheres,” *Int. J. Adv. Manuf. Technol.*, pp. 1–13, 2018.

[21] P. Bidare, I. Bitharas, R. M. Ward, M. M. Attallah, and A. J. Moore, “Fluid and particle dynamics in laser powder bed fusion,” *Acta Mater.*, vol. 142, pp. 107–120, 2018.

[22] S. Ly, A. M. Rubenchik, S. A. Khairallah, G. Guss, and J. Manyalibo, “Metal vapor micro-jet controls material redistribution in laser powder bed fusion additive manufacturing,” no. May, pp. 1–12, 2017.

[23] M. Simonelli *et al.*, “A Study on the Laser Spatter and the Oxidation Reactions During Selective Laser Melting of 316L Stainless Steel, Al-Si10-Mg, and Ti-6Al-4V,” *Metall. Mater. Trans. A Phys. Metall. Mater. Sci.*, vol. 46, no. 9, pp. 3842–3851, 2015.

[24] A. Ladewig, G. Schlick, M. Fisser, V. Schulze, and U. Glatzel, “Influence of the shielding gas flow on the removal of process by-products in the selective laser melting process,” *Addit. Manuf.*, vol. 10, pp. 1–9, 2016.

[25] M. Schniedenharn and J. H. Schleifenbaum, “On the Correlation of the Shielding Gas Flow in L-PBF Machines with Part Density,” no. March, pp. 1–7, 2018.

[26] B. Ferrar, L. Mullen, E. Jones, R. Stamp, and C. J. Sutcliffe, “Gas flow effects on selective laser melting (SLM) manufacturing performance,” *J. Mater. Process. Technol.*, vol. 212, no. 2, pp. 355–364, 2012.

[27] A. J. Dunbar and A. J. Dunbar, “Analysis of the Laser Powder Bed Fusion Additive Manufacturing Process Through Experimental Measurement and Finite Element Modeling,” *Thesis*, no. May, 2016.

[28] B. Lane, S. Moylan, E. P. Whitenton, and L. Ma, “Thermographic measurements of the commercial laser powder bed fusion process at NIST,” *Rapid Prototyp. J.*, vol. 22, no. 5, pp. 778–787, 2016.

[29] S. A. Khairallah, A. T. Anderson, A. Rubenchik, and W. E. King, “Laser powder-bed fusion additive manufacturing: Physics of complex melt flow and formation mechanisms of pores, spatter, and denudation zones,” *Acta Mater.*, vol. 108, pp. 36–45, 2016.

[30] J. Yang, H. Yu, J. Yin, M. Gao, Z. Wang, and X. Zeng, “Formation and control of martensite in Ti-6Al-4V alloy produced by selective laser melting,” *Mater. Des.*, vol. 108, pp. 308–318, 2016.

[31] L. Thijs, J. Van Humbeeck, K. Kempen, E. Yasa, and J. P. Kruth, “Investigation on the Inclusions in Maraging Steel Produced by Selective Laser Melting,” 1990.

[32] I. Yadroitsev and I. Yadroitsava, “Evaluation of residual stress in stainless steel 316L and Ti6Al4V samples produced by selective laser melting,” *Virtual Phys. Prototyp.*, vol. 10, no. 2, pp. 67–76, 2015.

[33] D. Wang, C. Song, Y. Yang, and Y. Bai, “Investigation of crystal growth mechanism during selective laser melting and mechanical property characterization of 316L stainless steel parts,” *Mater. Des.*, vol. 100, pp. 291–299, 2016.

[34] K. Saeidi, X. Gao, Y. Zhong, and Z. J. Shen, “Hardened austenite steel with columnar sub-grain structure formed by laser melting,” *Mater. Sci. Eng. A*, vol. 625, pp. 221–229, 2015.

[35] D. Giuranno, E. Arato, and E. Ricci, “Oxidation coditions of pure liquid metals and alloys,” *Chem. Eng. Trans.*, vol. 24, pp. 571–576, 2011.

[36] E. Hryha, E. Dudrova, and L. Nyborg, “On-line control of processing atmospheres for proper

sintering of oxidation-sensitive PM steels," *J. Mater. Process. Technol.*, vol. 212, no. 4, pp. 977–987, 2012.

[37] R. Li, J. Liu, Y. Shi, L. Wang, and W. Jiang, "Balling behavior of stainless steel and nickel powder during selective laser melting process," *Int. J. Adv. Manuf. Technol.*, vol. 59, no. 9–12, pp. 1025–1035, Apr. 2012.

[38] E. Hryha, R. Shvab, H. Gruber, A. Leicht, and L. Nyborg, "Surface Oxide State on Metal Powder and its Changes during Additive Manufacturing : an Overview," *La Metall. Ital.*, pp. 34–39, 2018.

[39] D. Herzog, V. Seyda, E. Wycisk, and C. Emmelmann, "Additive manufacturing of metals," *Acta Mater.*, vol. 117, pp. 371–392, 2016.

[40] A. Leicht, U. Klement, and E. Hryha, "Effect of build geometry on the microstructural development of 316L parts produced by additive manufacturing," *Mater. Charact.*, vol. 143, no. January, pp. 137–143, 2018.

[41] R. Casati, J. Lemke, and M. Vedani, "Microstructure and Fracture Behavior of 316L Austenitic Stainless Steel Produced by Selective Laser Melting," *J. Mater. Sci. Technol.*, vol. 32, no. 8, pp. 738–744, 2016.

[42] Y. Zhong, L. Liu, S. Wikman, D. Cui, and Z. Shen, "Intragranular cellular segregation network structure strengthening 316L stainless steel prepared by selective laser melting," *J. Nucl. Mater.*, vol. 470, no. November 2016, pp. 170–178, 2016.

[43] P. Krakhmalev *et al.*, "Microstructure, solidification texture, and thermal stability of 316 L stainless steel manufactured by laser powder bed fusion," *Metals (Basel).*, vol. 8, 2018.

[44] EOS, "Material data sheet - EOS StainlessSteel 316L," vol. 49, no. 0, pp. 1–5, 2014.

[45] Z. Jiang, H. Li, Z. Chen, Z. Huang, D. Zou, and L. Liang, "The Nitrogen Solubility in Molten Stainless Steel," *Steel Res. Int.*, vol. 76, no. September 2015, pp. 740–745, 2016.

[46] I. Woo and Y. Kikuchi, "Weldability of High Nitrogen Stainless Steel.," *ISIJ Int.*, vol. 42, no. 12, pp. 1334–1343, 2002.

[47] T. H. E. P. Goal and N. America, "Sintering and Corrosion Resistance," *Powder Metall. Stainl. Steels Process. Microstruct. Prop.*, pp. 60–100, 2007.

[48] J. A. Kitchener, J. O. M. Bockris, M. Gleiser, and J. W. Evans, "The solubility of oxygen in gamma iron," *Acta Metall.*, vol. 1, pp. 93–101, 1953.

[49] A. J. Cooper, W. J. Brayshaw, and A. H. Sherry, "Tensile Fracture Behavior of 316L Austenitic Stainless Steel Manufactured by Hot Isostatic Pressing," *Metall. Mater. Trans. A*, vol. 49, no. 5, pp. 1579–1591, 2018.

[50] X. Lou, P. L. Andresen, and R. B. Rebak, "Oxide inclusions in laser additive manufactured stainless steel and their effects on impact toughness and stress corrosion cracking behavior," *J. Nucl. Mater.*, vol. 499, pp. 182–190, 2018.

[51] Y. Zhang *et al.*, "On the Microstructures and Fatigue Behaviors of 316L Stainless Steel Metal Injection Molded with Gas- and," *Metals (Basel).*, vol. 8, no. 893, 2018.

[52] M. J. Donachie, Jr., "Titanium - A Technical Guide (2nd Edition)," *ASME Int.*, vol. 2, pp. 2–4, 2000.

[53] E. Hryha, R. Shvab, M. Bram, M. Bitzer, and L. Nyborg, "Surface chemical state of Ti powders and its alloys: Effect of storage conditions and alloy composition," *Appl. Surf. Sci.*, pp. 1–10, 2015.

[54] C. Qiu, N. J. E. Adkins, and M. M. Attallah, "Microstructure and tensile properties of selectively

laser-melted and of HIPed laser-melted Ti-6Al-4V," *Mater. Sci. Eng. A*, vol. 578, pp. 230–239, 2013.

[55] M. Simonelli, Y. Y. Tse, and C. Tuck, "Effect of the build orientation on the mechanical properties and fracture modes of SLM Ti-6Al-4V," *Mater. Sci. Eng. A*, vol. 616, pp. 1–11, 2014.

[56] EOS GmbH, "Material data sheet EOS Titanium Ti64 Material data sheet Technical data," vol. 49, no. 0, pp. 1–5, 2014.

[57] M. Yan *et al.*, "Review of effect of oxygen on room temperature ductility of titanium and titanium alloys Review of effect of oxygen on room temperature ductility of titanium and titanium alloys," vol. 5899, 2014.

[58] G. Lindwall, P. Wang, and U. R. Kattner, "The Effect of Oxygen on Phase Equilibria in the Ti-V System : Impacts on the AM Processing of Ti Alloys," *JOM*, vol. 70, no. 9, pp. 1692–1705, 2018.

[59] D. B. Lee, I. Pohrelyuk, O. Yaskiv, and J. C. Lee, "Gas nitriding and subsequent oxidation of Ti-6Al- 4V alloys," *Nanoscale Res. Lett.*, vol. 7, no. 1, p. 21, 2012.

[60] P. Pérez, "Influence of nitriding on the oxidation behaviour of titanium alloys at 700 C," *Surf. Coat. Technol.*, vol. 191, pp. 293–302, 2005.

[61] J. R. Davis, *Metals Handbook, Desk Edition (2nd Edition) - Bulk Elemental Analysis*. ASM International, 2015.

[62] ASTM- International, "ASTM E23-16b: Standard Test Methods for Notched Bar Impact Testing of Metallic Materials," *ASTM B. Stand.*, vol. i, pp. 1–26, 2016.

[63] ASTM-International, "ASTM B925-15: Standard Practices for Production and Preparation of Powder Metallurgy (P / M) Test," vol. 03, no. June, pp. 1–15, 2003.

[64] N. Pettersson, K. Frisk, and R. Fluch, "Materials Science & Engineering A Experimental and computational study of nitride precipitation in a CrMnN austenitic stainless steel," *Mater. Sci. Eng. A*, vol. 684, no. September 2016, pp. 435–441, 2017.

[65] T. Kurzynowski, E. Chlebus, B. Kuźnicka, and J. Reiner, "Parameters in selective laser melting for processing metallic powders," *Adv. Slow Fast Light V*, vol. 8239, pp. 1–6, 2012.

[66] C. Li, Z. Y. Liu, X. Y. Fang, and Y. B. Guo, "Residual Stress in Metal Additive," *Procedia CIRP*, vol. 71, pp. 348–353, 2018.